Canonical high power blazars

G. Ghiselini⋆ and F. Tavecchio
INAF – Osservatorio Astronomico di Brera, Via Bianchi 46, I–23807 Merate, Italy

29 May 2018

ABSTRACT

The jets of powerful blazars propagate within regions relatively dense of radiation produced externally to the jet. This radiation is a key ingredient to understand the origin of the high energy emission of blazars, from the X–ray to the γ–ray energy band. The main components contributing to the external radiation field are the accretion disk emission, including its X–ray corona, the broad line region, the infrared emitting torus and the cosmic background radiation. Their importance changes as a function of the distance from the black hole and of the value of the bulk Lorentz factor of the jet. These external radiation fields control the amount of the inverse Compton radiation with respect to the synchrotron flux. Therefore the predicted spectral energy distribution (SED) will depend on where the jet dissipates part of its energy to produce the observed radiation. We investigate in detail how the SED changes as a function of the location of the jet dissipation region, by assuming rather "standard" (i.e. "canonical") prescriptions for the accretion disk and its X–ray corona, the profile of the jet magnetic field and the external radiation. We confirm that most of the dissipation, if producing the γ–ray flux we see, must occur at hundreds of Schwarzschild radii from the black hole, to avoid the γ–$\gamma \to e^{\pm}$ process, and the consequent re–emission by the produced pairs. The magnetic energy density of a "canonical" jet almost never dominates the radiative cooling of the emitting electrons, and consequently the inverse Compton flux almost always dominates the bolometric output. This is more so for large black hole masses. Dissipation taking place beyond the broad line region is particularly interesting, since it accounts in a simple way for the largest inverse Compton to synchrotron flux ratios accompanied by an extremely hard X–ray spectrum. Furthermore it makes the high power blazars at high redshift useful tools to study the optical to UV cosmic backgrounds.

Key words: BL Lacertae objects: general — quasars: general — radiation mechanisms: non-thermal — gamma-rays: theory — X-rays: general

1 INTRODUCTION

Relativistic jets in blazars transport energy in the form of bulk motion of protons, leptons and magnetic field. When part of this power is dissipated, the particles emit the beamed radiation we observe, consisting of two broad humps. The origin of the low frequency hump is well established, believed to be synchrotron radiation from relativistic (in the comoving frame) leptons. The nature of the high energy hump is a controversial issue. In general, we can group the existing models into three families: i) the high energy radiation is generated by the same leptons producing the synchrotron, through the inverse Compton process (Maraschi, Ghisellini & Celotti 1992; Dermer & Schlickeiser 1993; Sikora, Begelman & Rees 1994; Ghisellini & Madau 1996; Bloom & Marscher 1996; Celotti & Ghisellini 2008); ii) There are two populations of leptons, one accelerated directly by the acceleration mechanism (i.e. shocks), and a second one resulting from cascades initiated

by ultra–relativistic protons (Mannheim 1993; Mücke et al. 2003; Böttcher 2007); iii) Ultrarelativistic protons emit by the proton–synchrotron process at high energies (Aharonian 2000; Mücke & Protheroe 2001).

Another issue of debate is the role of electron–positron pairs. Sikora & Madejski (2000) discussed this problem concluding that, though they can exist, their amount is limited to a few pairs per proton, and a similar conclusion was reached by Celotti & Ghisellini (2008) analysing a large number spectral energy distributions (SEDs) for deriving the jet powers of blazars. This contrasts the idea, originally put forward by Blandford & Levinson (1995) that the γ–rays spectrum is the superposition of the spectra originating at different distances from the black hole, each one cutted–off at a different γ–ray energy as a result of photon–photon absorption. In this scheme a large amount of pairs is produced, since the high energy hump carries most of the emitted power: if this is partly absorbed, we transform most of the total power into (energetic) pairs.

Ghisellini & Madau (1996) argued that the Blandford & Levinson idea has one important observational consequence in

powerful blazars with a standard accretion disk: since the pairs are born relativistic, they contribute to the emission mainly by inverse Compton scattering the dense UV radiation field coming from the accretion disk. In fact, if we want the emission region be compact, it is reasonable to locate it close to the accretion disk and its X–ray corona. This implies that the coronal X–rays are targets for the γ–$\gamma \to e^{\pm}$ process, and that the accretion disk UV photons become seeds for the scattering made by the newly born pairs. The resulting radiation is mainly in the X–ray band, that should have a power comparable to the power absorbed in the γ–ray band, contrary to what observed. This led Ghisellini & Madau (1996) to conclude that the dissipation region in blazar jets cannot be very close to the accretion disk. On the other hand the observed fast variability argues for not too large distances. Taken together, these two limits strongly suggest that there is a preferred distance at which *the γ–ray radiation is produced*, at some hundreds of Schwarzschild radii. Since this argument makes use of the reprocessed radiation produced by the pairs, it cannot be applied when most of the radiation is produced below the pair production energy threshold and/or if the accretion disk is radiatively inefficient: in both cases very few pairs are created. Indeed, Katarzynski & Ghisellini (2007) proposed a jet model in which a dissipation close to the accretion disk resulted in a low level γ–ray emission, with no contradiction with the existing X–ray data.

These arguments, although correct, are qualitative, and in our opinion a detailed computation of the reprocessing due to pairs is not yet present in the literature. Therefore one of the aims of the present paper is to derive some limits on the location of the dissipation region in the jet of powerful blazars. We will do it in the framework of the "leptonic" class of models [family i) mentioned above], and we limit our analysis to blazars having a "standard" (Shakura & Sunyaev 1973) accretion disk. This implies to consider Flat Spectrum Radio Quasars (FSRQs, and their likely parent population, FR II radio–galaxies) and not BL Lac objects, that are likely to have radiatively inefficient accretion flows (see Celotti & Ghisellini 2008 and Ghisellini & Tavecchio 2008 for more discussion about this point).

While doing this, we will study the relative importance of different sources of seed photons as a function of the distance $R_{\rm diss}$ of the dissipation region from the black hole, and their spectrum as seen in the comoving frame. This is the second aim of the paper. Besides the radiation coming directly from the accretion disk and its X–ray corona, we will consider the radiation produced in the Broad Line Region (BLR) and in a relatively more distant dusty torus, intercepting a fraction of the disk radiation and re–emitting it in the infrared. Finally, we also include the contribution of the Cosmic Microwave Background (CMB), important for very large (beyond 1 kpc) $R_{\rm diss}$.

The term "canonical high power blazars" refers to the rather standard choice for both the environment of these sources and their jets:

(i) The accretion disk is a standard, "Shakura & Syunyaev" (1973) disk.

(ii) Above this accretion disk, there is an X–ray corona, emitting a luminosity less than, but comparable to, the luminosity emitted by the accretion disk.

(iii) the BLR and the IR torus are located at distances that scale as the square root of the disk luminosity (Bentz et al. 2006; Kaspi et al. 2007; Bentz et al. 2008; see the discussion about this point made in Ghisellini & Tavecchio 2008).

(iv) The jet is assumed to dissipate only a fraction of its total power, which is then conserved. After the acceleration phase, possibly magnetic in origin, we assume that also the Poynting flux is conserved (see e.g. Celotti & Ghisellini 2008).

Our study is not completely new, since several of its "ingredients" have already been discussed in the literature. The paper more german to our is Dermer et al. (2009), but we include some new ingredients. The novel features of our investigation concern mainly: i) the inclusion of the X–ray corona as an important producer of target photons for the γ–$\gamma \to e^{\pm}$ process; ii) the calculation of the emitting particle distribution, including pair creation; iii) the effects of jet acceleration at small distances from the black hole; iv) the strict link between the properties of the accretion disk and the amount of the external radiation and v) the overall scenario allowing to describe in a more general way (than done before) the SED properties of high power jets at all scales.

The paper is divided into four parts. In the first we study the different sources of external radiation, and the corresponding energy densities, as seen in the comoving frame, as a function of distance from the black hole and as a function of the bulk Lorentz factor of the jet. In the second part of the paper we investigate the role of pair production processes when the dissipation region is close to the black hole, with the aim to find quantitative constraints. In the third part we construct the expected SED as a function of distance, highlightening what are the relevant external seed photons. Finally, in the fourth part, we apply some of the above results and considerations when modelling the SED of some blazars, used as illustrative examples, and we check if our scenario can reproduce the phenomenological blazar sequence (Fossati et al. 1998).

We use a cosmology with $h_0 = \Omega_\Lambda = 0.7$ and $\Omega_{\rm M} = 0.3$. We also use the notation $Q = 10^x Q_X$ in cgs units, unless noted otherwise.

2 SETUP OF THE MODEL

Our model is characterised by the following setup. The accretion disk extends from $R_{\rm in} = 3R_{\rm S}$ to $R_{\rm out} = 500R_{\rm S}$ ($R_{\rm S}$ is the Schwarzschild radius) and is producing a total luminosity $L_{\rm d} = \eta \dot{M} c^2$, where $\dot{M}$ is the accretion rate and η is the accretion efficiency. Locally, its emission is black–body, with a temperature

$$T^4 = \frac{3R_{\rm S}L_{\rm d}}{16\pi\eta\sigma_{\rm MB}R^3}\left[1 - \left(\frac{3R_{\rm S}}{R}\right)^{1/2}\right] \qquad (1)$$

Below and above the accretion disk there is a hot corona, emitting UV and X–rays with a luminosity $L_X = f_X L_{\rm d}$. For simplicity, the corona is assumed to be homogeneous between 3 and 30 Schwarzschild radii. The spectrum is assumed to be a cut–off power law: $L_X(\nu) \propto \nu^{-\alpha_X} \exp(-\nu/\nu_{\rm c})$.

The broad line region (BLR) is assumed to be a shell located at a distance

$$R_{\rm BLR} = 10^{17} L_{\rm d,45}^{1/2} \text{ cm} \qquad (2)$$

It reprocesses a fraction $f_{\rm BLR}$ of $L_{\rm d}$ in lines, especially the hydrogen Lyman–α line, and continuum. Following Tavecchio & Ghisellini (2008), we assume that the spectral shape of the BLR observed in the comoving frame is a black–body peaking at a factor Γ times the (rest frame) frequency of the Lyman–α line.

We also assume the presence of a torus (see Błazejowski et al. 2000; Sikora et al. 2002), at a distance

$$R_{\rm IR} = 2.5 \times 10^{18} L_{\rm d,45}^{1/2} \text{ cm} \qquad (3)$$

reprocessing a fraction f_{IR} of the disk radiation in the infrared. Note that both R_{BLR} and R_{IR} scale as the square root of L_d: this implies that, in the lab frame, the radiation energy densities of these two components are constant, as long as R_{diss} is smaller than these two radii. We emphasise that our treatment of the torus emission is approximate: it is likely that the torus itself is a complex structure, possibly clumpy (Nenkova et al. 2008) with a range of radii, extending also quite close to the black hole, where the temperature is just below dust sublimation (i.e. ~ 1500 K). Our approach follows in part the results of Cleary et al. (2007), finding weak signs of hot dust emission in the studied spectra, and partly is dictated by simplicity.

The emitting region is moving with a velocity βc corresponding to a bulk Lorentz factor Γ. We call R_{diss} the distance of the dissipation region from the black hole. We consider either a constant Γ or include an acceleration phase of the kind (see e.g. Komissarov et al. 2007; Vlahakis & Königl 2004):

$$\Gamma = \min \left[\Gamma_{max}, \left(\frac{R}{3R_S} \right)^{1/2} \right] \tag{4}$$

When the acceleration phase is taken into account, the jet is assumed to be parabolic in shape, becoming conical when Γ reaches its maximum value (see e.g. Vlahakis & Königl 2004). Calling r the cross sectional radius of the jet, and R the distance from the black hole, we have

$$r = \phi R^{1/2}, \quad \Gamma \leqslant \Gamma_{max}$$
$$r = \psi R, \qquad \Gamma \geqslant \Gamma_{max} \tag{5}$$

where ψ is the semi–aperture angle of the jet in its conical part, and the constant ϕ is fixed by assuming that at the start of the jet we have $r_o = R_0 = 3R_S$. The parabolic and conical parts of the jet connect at $R = 3R_S\Gamma_{max}^2$.

The total power carried by the jet, P_j, was assumed in Ghisellini & Tavecchio (2008) to be related to the mass accretion rate, i.e. $P_j = \eta_j \dot{M} c^2$. Since Celotti & Ghisellini (2008) found that P_j is greater than the disk accretion luminosity, i.e. $P_j \gtrsim L_d$, we assumed (in Ghisellini & Tavecchio 2008) that η_j was greater than the corresponding efficiency of transforming the accretion rate $\dot{M}$ in disk luminosity. When fitting the data of specific sources, we do not specify a priori the total jet luminosity, which is instead a result of the modelling (once we assume how many protons there are for each emitting lepton). Therefore P_j is not an input parameter in our scheme, but is a quantity derived a posteriori. What we will specify, instead, is the power injected in the dissipation region, that is related to the power carried by the jet in relativistic electrons (and by cold protons, once we specify how many protons there are per emitting electron).

We assume a value of the magnetic field in the dissipation region, that corresponds to a Poynting flux P_B. If the jet is magnetically accelerated, then the initial (i.e. close to R_0) P_B should be of the same order of P_j, becoming $P_B = \epsilon_B P_j = $ const when Γ reaches its maximum value. To describe the profile of P_B we assume the following prescription:

$$P_B = \pi r^2 \Gamma^2 c U_B = P_j \left[1 - \frac{\Gamma \beta}{\Gamma_{max}\beta_{max}} (1 - \epsilon_B) \right] \tag{6}$$

In this way $P_B = P_j$ initially, becoming a constant fraction ϵ_B of P_j when the jet is conical. Here $U_B = B^2/(8\pi)$ is the magnetic energy density.

The energy distribution of the particles responsible for the emission is derived through the continuity equation, assuming a continuous injection of particles throughout the source lasting for a finite time. This time is the light crossing time $t_{cross} = r_{diss}/c$, where r_{diss} is the size of the emitting blob, located at the distance R_{diss} from black hole. We always calculate the particle distribution at this time. The reason for this approach is suggested by the fast variability shown by blazars, indicating that the release of energy is short and intermittent. Besides, we believe that this approach is the simplest that can nevertheless describe in some detail the particle distribution. In fact, it allows to neglect: i) adiabatic losses (important after r_{diss}/c, which is also the time needed to double the radius); ii) particle escape (again important for times longer than r_{diss}/c) and iii) the changed conditions in the emitting region (since the source is travelling and expanding, the magnetic field changes).

High energy particles can radiatively cool in a time shorter than t_{cross}. Let us call γ_{cool} the energy of those particles halving their energy in a time t_{cross}. Above γ_{cool}, and at $t = t_{cross}$, the particle energy distribution $N(\gamma, t_{cross})$ can be found by solving

$$\frac{\partial}{\partial \gamma} [\dot{\gamma} N(\gamma, t_{cross})] + Q(\gamma) + P(\gamma) = 0 \tag{7}$$

where $\dot{\gamma}$ is the cooling rate of a particle of energy $\gamma m c^2$, $Q(\gamma)$ is the source term (i.e. the injection of primary particles) assumed constant in time, and $P(\gamma)$ is the term corresponding to the electron–positron pairs that are produced in photon–photon collisions. The formal solution of Eq. 7 is

$$N(\gamma) = \frac{\int_\gamma^{\gamma_{max}} [Q(\gamma) + P(\gamma)] d\gamma}{\dot{\gamma}}, \quad \gamma > \gamma_{cool} \tag{8}$$

When electrons with $1 < \gamma < \gamma_{cool}$ do not cool in t_{cross} we approximate the low energy part of $N(\gamma)$ with

$$N(\gamma) \sim t_{cross}[Q(\gamma) + P(\gamma)], \quad \gamma < \gamma_{cool} \tag{9}$$

Note that, within our assumptions, the particle distribution of Eq. 8 and Eq. 9 correspond to the maximum $N(\gamma)$. The injection of primary particles $Q(\gamma)$ is a smoothly joining broken power law:

$$Q(\gamma) = Q_0 \frac{(\gamma/\gamma_b)^{-s_1}}{1 + (\gamma/\gamma_b)^{-s_1+s_2}} \tag{10}$$

where γ_b is a break energy. The pair injection term $P(\gamma)$ corresponds to the γ–$\gamma \to e^\pm$ process only, and it is calculated with the prescriptions given by Svensson (1987) and Ghisellini (1989).

The total power injected in the form of relativistic electrons, calculated in the comoving frame, is

$$P_i' = m_e c^2 V \int_1^{\gamma_{max}} \gamma Q(\gamma) d\gamma \tag{11}$$

where $V = (4\pi/3) r_{diss}^3$ is the emitting volume. Note that this is not equivalent to the power that the jet transports in the form of relativistic particles (as measured in the comoving frame), since P_i' includes also the energy that will be emitted, and possibly transformed into pairs.

3 ENERGY DENSITIES

3.1 Direct disk radiation

Each annulus of the accretion disk is characterised by a different temperature and it is seen under a different angle ξ (with respect to the jet axis), thus its radiation is boosted in a different way. A
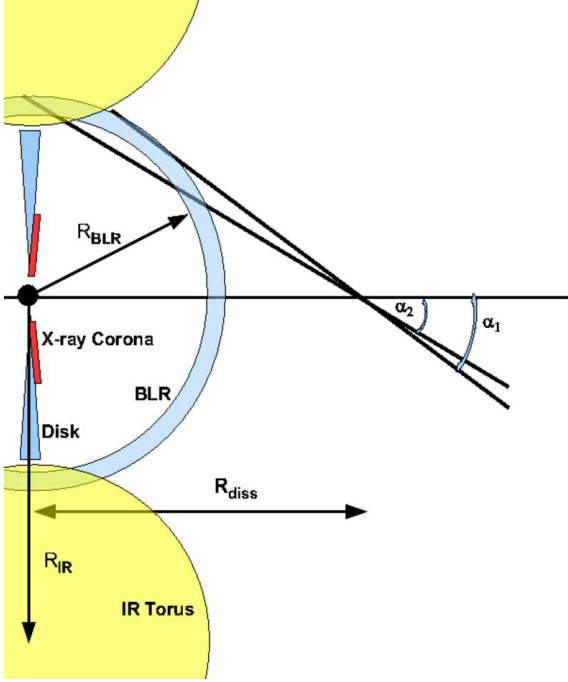
Figure 1. Cartoon illustrating the accretion disk, its X–ray corona, the broad line region and a schematic representation of the IR torus. At the distance $R_{\rm diss}$ the jet is assumed to dissipate. At this distance, here assumed to be outside the BLR, we label the relevant angles for calculating the contribution of the BLR radiation to the corresponding energy density.

stationary observer with respect to the black hole (lab frame) will see a flux, integrated over all annuli, given by

$$F_{\rm d}(\nu) = 2\pi \int_{\mu_{\rm d}}^{1} I(\nu)d\mu = 2\pi \int_{\mu_{\rm d}}^{1} \frac{2h\nu^3/c^2}{\exp[h\nu/(kT)]-1}d\mu \tag{12}$$

where $\mu = \cos\xi$, and $\mu_{\rm d}$ is given by

$$\mu_{\rm d} = [1 + R_{\rm out}^2/R_{\rm diss}^2]^{-1/2} \tag{13}$$

In the comoving frame of the blob, frequency are transformed as:

$$\nu' = b\nu, \qquad b \equiv \Gamma(1-\beta\mu) \tag{14}$$

and solid angles transform as:

$$d\Omega' = \frac{d\Omega}{b^2} = 2\pi\frac{d\mu}{b^2} \tag{15}$$

where primed quantities are in the comoving frame. The intensities as seen in the comoving frame transform as:

$$I'_{\rm d}(\nu') = b^3 I_{\rm d}(\nu) = b^3 I_{\rm d}(\nu'/b) \tag{16}$$

The specific radiation energy density seen in the comoving frame is

$$U'_{\rm d}(\nu') = \frac{1}{c}\int I'_{\rm d}(\nu')d\Omega' = \frac{2\pi}{c}\int_{\mu_{\rm d}}^{1} \frac{I'_{\rm d}(\nu')}{b^2}d\mu \tag{17}$$

3.2 Radiation from the X–ray corona

According to our assumptions, the total radiation energy density U'_X of this component is (see e.g. Ghisellini & Madau 1996):

$$U'_X = \frac{f_X L_{\rm d}\Gamma^2}{\pi R_X^2 c}\left[1 - \mu_X - \beta(1-\mu_X^2) + \frac{\beta^2}{3}(1-\mu_X^3)\right]$$

$$\mu_X = [1 + R_X^2/R_{\rm diss}^2]^{-1/2} \tag{18}$$

where R_X is the extension of the X–ray corona.

3.3 BLR radiation

Within $R_{\rm BLR}$ the corresponding energy density seen in the comoving frame can be approximated as (Ghisellini & Madau 1996):

$$U'_{\rm BLR} \sim \frac{17\Gamma^2}{12}\frac{f_{\rm BLR}L_{\rm d}}{4\pi R_{\rm BLR}^2 c} \qquad R_{\rm diss} < R_{\rm BLR} \tag{19}$$

At distances much larger than $R_{\rm BLR}$, and calling $\mu = \cos\alpha$, we have (see the cartoon in Fig. 1)

$$U'_{\rm BLR} \sim \frac{f_{\rm BLR}L_{\rm d}}{4\pi R_{\rm BLR}^2 c}\frac{\Gamma^2}{3\beta}[2(1-\beta\mu_1)^3 - (1-\beta\mu_2)^3$$

$$- (1-\beta)^3)] \qquad R_{\rm diss} \gg R_{\rm BLR}$$

$$\mu_1 = [1 + R_{\rm BLR}^2/R_{\rm diss}^2]^{-1/2}$$

$$\mu_2 = [1 - R_{\rm BLR}^2/R_{\rm diss}^2]^{1/2} \tag{20}$$

For $R_{\rm diss} \gtrsim R_{\rm BLR}$ the exact value of $U'_{\rm BLR}$ depends on the width of the BLR, which is poorly known. For this reason, in the range $R_{\rm BLR} < R_{\rm diss} < 3R_{\rm BLR}$ we use a simple (power–law) interpolation.

The BLR is assumed to "reflect" (Compton scatter) a fraction $f_{\rm BLR,X}$ (of the order of 1 per cent) of the corona emission. The existence of this diffuse X–ray radiation is a natural outcome of photo–ionisation models for the BLR (see e.g. Tavecchio & Ghisellini 2008, Tavecchio & Mazin 2009). The assumed value, $f_{BLR,X} \sim 0.01$, is the average value found for typical parameters of the clouds.

3.4 Radiation from the IR torus

This component scales as $U_{\rm BLR}$, but substituting $R_{\rm BLR}$ with $R_{\rm IR}$. We have

$$U'_{\rm IR} \sim \frac{f_{\rm IR}L_{\rm d}\Gamma^2}{4\pi R_{\rm IR}^2 c} \qquad R_{\rm diss} < R_{\rm IR} \tag{21}$$

For $R_{\rm diss} > R_{\rm IR}$ we have the same behaviour as in Eq. 20, but with $R_{\rm IR}$ replacing $R_{\rm BLR}$. In a νF_ν plot the (lab frame) peak frequency of this component is assumed to be at $\nu_{\rm IR} = 3 \times 10^{13}$ Hz (see Cleary et al. 2007), independent of the disk luminosity, since $R_{\rm IR}$ scales as $L_{\rm d}^{1/2}$. The corresponding temperature is $T_{\rm IR} = h\nu_{\rm IR}/(3.93k)$ (we must use the factor 3.93, instead of the usual 2.82, because we are using the peak frequency in νF_ν). In the comoving frame this corresponds to

$$T'_{\rm IR} \sim 370\,b \text{ K} \tag{22}$$

3.5 Radiation from the host galaxy bulge

The bulge of the galaxy hosting the blazar can be a non–negligible emitter of ambient optical radiation (see e.g. (Stawarz, Sikora & Ostrowski 2003). Within the bulge radius $R_{\rm star}$ emitting a luminosity $L_{\rm star}$ we have

$$U'_{\rm star} = \Gamma^2 \frac{L_{\rm star}}{4\pi R_{\rm star}^2 c} \tag{23}$$

As an order of magnitude estimate, we have $U'_{\rm star} \sim 10^{-10}\Gamma^2$ erg cm^{-3} using $L_{\rm star} = 3 \times 10^{44}$ erg s^{-1} produced within a bulge radius $R_{\rm star} \sim 1$ kpc. When $R_{\rm diss} > R_{\rm star}$, $U'_{\rm star}$ decreases in an analogous way as $U'_{\rm IR}$ and $U'_{\rm BLR}$ (once we substitute $R_{\rm star}$ to $R_{\rm IR}$ or $R_{\rm BLR}$).

3.6 Radiation from the cosmic background

The energy density of the Cosmic Background Radiation (CMB), as seen in the comoving frame, is

$$U'_{\rm CMB} \ = \ aT_0^4\Gamma^2(1+z)^4 \tag{24}$$

where $a = 7.65 \times 10^{-15}$ erg cm^{-3} deg^{-4} and $T_0 = 2.7$ K is the temperature of the CMB now (i.e. at $z = 0$).

3.7 Magnetic field

Following our prescriptions concerning the power carried in the form of Poynting flux, we have

$$U'_{\rm B} \ = \ \frac{P_{\rm B}}{\pi r_{\rm diss}^2\Gamma^2 c} \ = \ \frac{P_{\rm j}}{\pi r_{\rm diss}^2\Gamma^2 c}\left[1 - \frac{\Gamma\beta}{\Gamma_{\max}\beta_{\max}}\left(1 - \epsilon_{\rm B}\right)\right] \tag{25}$$

The magnetic field B scales as $1/R_{\rm diss}$ both in the acceleration and in the coasting (i.e. $\Gamma =$const) phases, but with a different normalisation.

3.8 Internal radiation

This component corresponds mainly to the radiation produced by the blob that can be efficiently scattered through the inverse Compton process. This cannot be calculated without specifying the relativistic particle distribution. If the emitting volume V is a sphere, the synchrotron radiation energy density formally is:

$$
\begin{aligned}
U'_{\rm syn} \ &= \ \frac{V}{4\pi r_{\rm diss}^2 c}m_e c^2 \int N(\gamma)\dot{\gamma}_{\rm syn}d\gamma \\
&= \ \frac{4}{9}[nr_{\rm diss}\sigma_{\rm T}]U'_{\rm B}\frac{\int N(\gamma)\gamma^2 d\gamma}{\int N(\gamma)d\gamma} \\
&= \ \frac{4}{9}[nr_{\rm diss}\sigma_{\rm T}\langle\gamma^2\rangle]U'_{\rm B} \ = \ \frac{4}{9}\,y\,U'_{\rm B} \tag{26}
\end{aligned}
$$

where $\sigma_{\rm T}$ is the Thomson cross section, n is the number density of the emitting particles and $y \equiv \sigma_{\rm T}nr_{\rm diss}\langle\gamma^2\rangle$ is the relativistic Comptonization parameter. This parametrisation follows the one in Ghisellini & Tavecchio (2008). From the fits to a sample of blazars performed in Celotti & Ghisellini (2008) we have that y is in the range 0.1–10. Since the found distribution of y values is rather narrow, one has a first order estimate of what is the internal radiation through the value and profile of the magnetic energy density $U_{\rm B}$.

3.9 Comparing the different components

We have calculated the contributions to the energy density given by the different components as a function of $R_{\rm diss}$, plotting them in Fig. 2. For these cases, we have chosen a black hole mass $M = 10^9 M_\odot$, an accretion disk extending from $3R_s$ to $500R_{\rm S}$, an accretion efficiency $\eta = 0.08$, $f_{\rm BLR} = f_X = 0.1$, $f_{\rm IR} = 0.5$. We plot the results for two values of $L_{\rm d}$: 10^{45} and 10^{47} erg s^{-1}. In the top panel we show the case of an accelerating jet, whose bulk Lorentz factor is $\Gamma = \min[15, (R_{\rm diss}/3R_{\rm S})^{1/2}]$. In the bottom panel we assume a constant $\Gamma = 15$ along the entire jet. As can be seen, the dominant energy density is different at different $R_{\rm diss}$. As a rule, all the external radiation energy densities drop when $R_{\rm diss}$ is greater than the corresponding typical size of the structure producing the seed photons.

Particularly interesting is the comparison between $U'_{\rm d}$ and $U'_{\rm BLR}$. The distance above which $U'_{\rm BLR} > U'_{\rm d}$ depends upon the
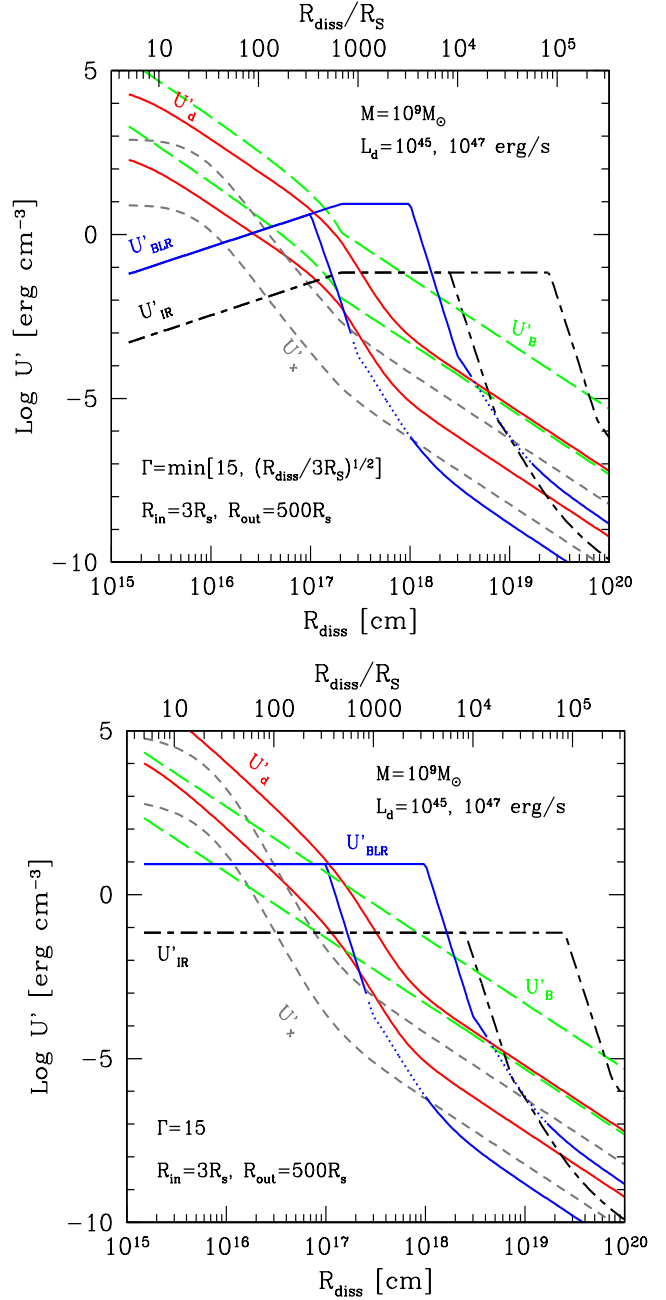
Figure 2. Top panel: Comparison of different energy densities as measured in the comoving frame. The moving blob is assumed to have a bulk Lorentz factor $\Gamma = \min[15, (R_{\rm diss}/3R_{\rm S})^{1/2}]$. The black hole has a mass $M = 10^9 M_\odot$. The different contributions are labelled. The disk emits as a blackbody, and extends from 3 to 500 Schwarzschild radii. The two sets of lines correspond to two disk luminosities: 10^{45} and 10^{47} erg s^{-1}. The radius of the broad line region is assumed to scale with the disk luminosity as $R_{\rm BLR} = 10^{17}L_{\rm d,45}^{1/2}$ cm. The radius of the IR torus scales as $R_{\rm IR} = 2.5 \times 10^{18}L_{\rm d,45}^{1/2}$ cm. The X–ray corona is assumed to be homogeneous, to extend up to 30 Schwarzschild radii and to emit 10 per cent of the disk luminosity. The contribution of the BLR between 1 and 3 $R_{\rm BLR}$ depends on the unknown width of the BLR itself (dotted line). The magnetic energy density (long dashed lines) is calculated assuming $P_{\rm j} = L_{\rm d}$ and $\epsilon_{\rm B} = 0.1$. Bottom panel: as above, but assuming a constant $\Gamma = 15$ all along the jet.
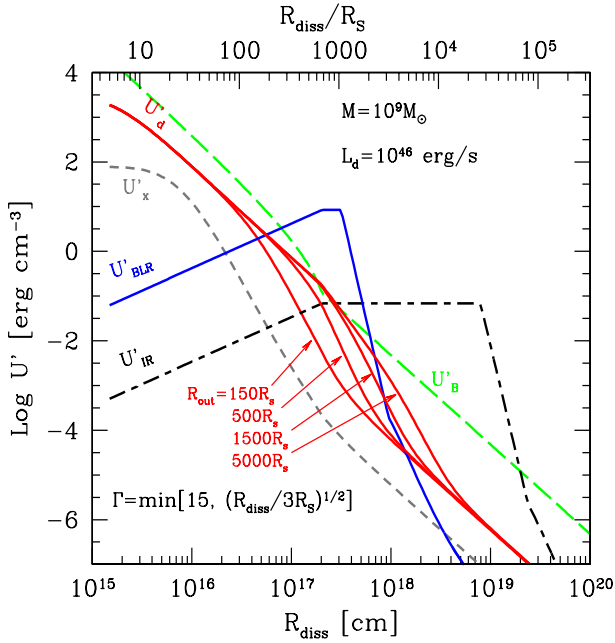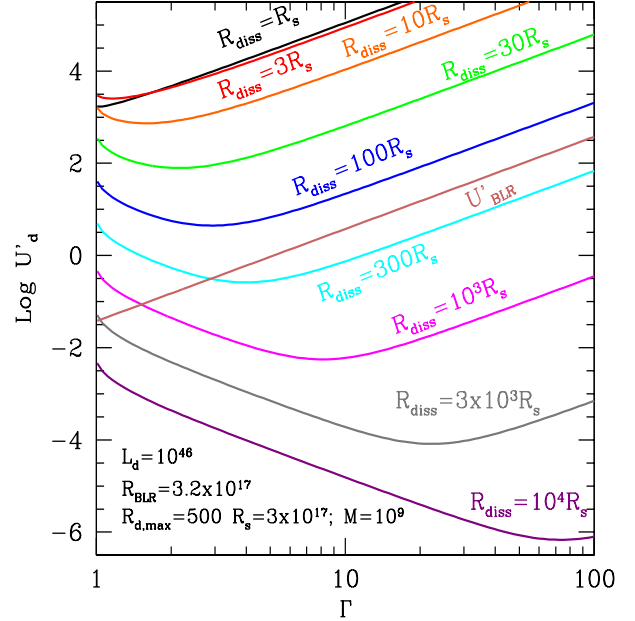
Figure 3. The energy density as seen in the comoving frame of the blob, moving with a bulk Lorentz factor $\Gamma = \min[15, (R_{\mathrm{diss}}/3R_{\mathrm{S}})^{1/2}]$. The black hole has a mass $M = 10^9 M_\odot$, and the disk emit $L_{\mathrm{disk}} = 10^{46}$ erg s^{-1}. The different contributions are labelled. This figure shows the effect of changing the outer radius of the accretion disk, from 150 to 5000 R_{S}, as indicated by the labels and arrows. As the outer radius increases, U_{d}' increases at distances $R_{\mathrm{diss}} \sim R_{\mathrm{out}}$, but there the disk contribution is overtaken by U_{BLR}' and U_{IR}'.

disk luminosity, since the BLR adjusts its radius so to give a constant (in the lab frame) energy density. So for $L_{\mathrm{d}} = 10^{47}$ erg s^{-1} the energy density from the BLR dominates only above 10^{17} cm, equivalent to $\sim 300 R_{\mathrm{S}}$, while for $L_{\mathrm{d}} = 10^{45}$ erg s^{-1} it starts to dominate about three times closer, when Γ has not reached yet its maximum value. Note that, for the shown cases, U_{B}' dominates over the external radiation energy density only at the start of the jet and up to 100–300 R_{S}, where U_{BLR}' takes over. In this particular examples, we assumed $P_{\mathrm{B}} = 0.1 L_{\mathrm{d}}$.

Fig. 3 illustrates the effects of changing the outer radius of the accretion disk, from $R_{\mathrm{out}} = 150$ to 5000 Schwarzschild radii. As expected, U_{d}' remains the same at small and very high distances, and increases with R_{out} in between, at distances comparable with R_{out}. The increase of U_{d}' is modest, and occurs when the external radiation energy density is dominated by the BLR and torus components.

In Fig. 4 we show U_{d}' as a function of Γ for different locations of the dissipation region. Of course the largest U_{d}' are obtained when the source is very close to the accretion disk. For each R_{diss} there is a value of Γ that minimises U_{d}'. To understand this (somewhat anti–intuitive) behaviour we must recall that the boosting factor $b = \Gamma(1 - \beta\mu)$ has a minimum for $\beta = \mu$. This corresponds, in a comoving frame, to $\mu' = 0$, i.e. an angle of $90°$. Therefore, when the external radiation is all coming from a ring, we expect that in the comoving frame, the radiation energy density initially decreases increasing β, but when the photons are starting to come from the forward hemisphere (i.e. $\mu' < 0$, or, equivalently, $\mu < \beta$), U_{d}' increases increasing β. This explains the minima shown in Fig.
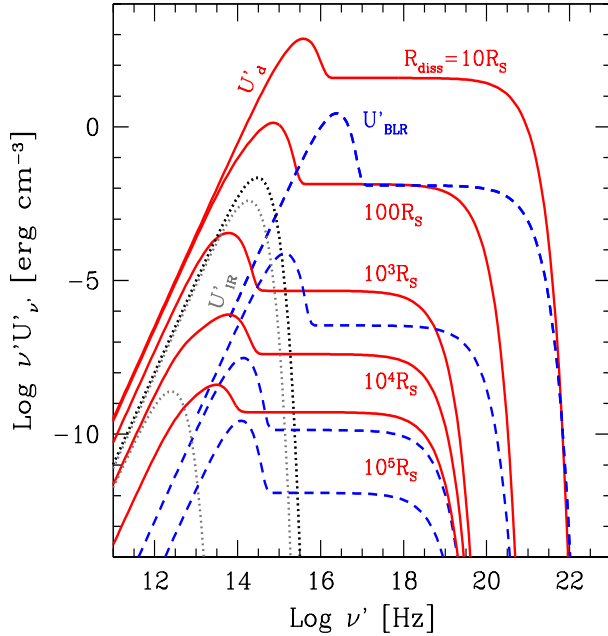

Figure 4. The radiation energy density U_{d}' (as seen in the comoving frame) produced by the direct radiation of the accretion disk as a function of Γ, for different distances R_{diss}, for a total disk luminosity $L_{\mathrm{d}} = 10^{46}$ erg s^{-1} and a black hole mass $M = 10^9 M_\odot$. For comparison we show the radiation energy density observed *within* the BLR. It can be directly compared with U_{d}' only for $R_{\mathrm{diss}} < R_{\mathrm{BLR}}$.

4, once we weight the above effect with the intensity produced at each ring.

3.10 Spectra of the external radiation

Besides comparing the frequency integrated components forming the radiation energy density in the comoving frame, it is instructive to compare also their different spectra. This is because the Doppler boost appropriate for each component is not the same, and it changes for different distances from the black hole. In Fig. 5 we show one illustrative example, calculated for a blob moving with a constant $\Gamma = 15$ and located at different R_{diss}. The disk is assumed to emit $L_{\mathrm{d}} = 10^{45}$ erg s^{-1} and the black hole mass is $M = 10^9 M_\odot$, corresponding to $R_{\mathrm{S}} = 3 \times 10^{14}$ cm. With this disk luminosity, the BLR is located at $R_{\mathrm{BLR}} = 10^{17}$ cm, implying that for $R_{\mathrm{diss}} < R_{\mathrm{BLR}}$ the radiation energy density from the BLR is the same. For larger R_{diss} the total U_{BLR}' decreases (see Eq. 20). The radiation energy density from the disk and its corona always decreases increasing R_{diss}, being larger than U_{BLR}' for $R_{\mathrm{diss}} < 100 R_{\mathrm{S}} \sim 3 \times 10^{16}$ cm (see also Fig. 2). The disk radiation dominates again for $R_{\mathrm{diss}} \gtrsim \times 10^{18}$ cm (see Fig. 2). For small R_{diss}, the high energy X–ray photons coming from the corona will be responsible of a large optical depth for the γ–γ process, as discussed below. The IR energy density coming form the torus is constant for all R_{diss} but for the largest value (since $R_{\mathrm{IR}} = 8.3 \times 10^3 R_{\mathrm{S}} = 2.5 \times 10^{18}$ cm). This component will be larger than U_{d}' and U_{BLR}' for R_{diss} greater than $\sim 500 R_{\mathrm{S}} \sim 2 \times 10^{17}$ cm.

Figure 5. The spectra of the radiation energy density (as seen in the co-moving frame) produced by the direct disk plus the X–ray corona (U'_d, solid line), the BLR (U'_BLR, including the "reflected" X–rays, dashed line) and the IR torus (U'_IR, dotted line). We have assumed a constant $\Gamma = 15$, $M = 10^9 M_\odot$ and $L_\mathrm{d} = 10^{45}$ erg s^{-1}. The spectra are shown for 5 different R_diss. For $R_\mathrm{diss} = 10$ and 100 Schwarzschild radii $U'_\mathrm{BLR}(\nu')$ is the same, since for these cases $R_\mathrm{diss} < R_\mathrm{BLR}$. The contribution of the IR emitting torus is the same up to $R_\mathrm{diss} = 10^3 R_\mathrm{S}$, and starts to decline afterwards, when $R_\mathrm{diss} > R_\mathrm{IR}$.

3.11 Input parameters

Having included many components of external radiation, and having tried to link the jet emission to the accretion disk luminosity and the black hole mass, we necessarily have a large numbers of parameters for a specific model. It can be useful to summarise them here, dividing them into two separated lists. In the latter we have those parameters that we fix for all models, based on physical considerations or a priori knowledge, or that do not influence the model SED (apart from pathological cases); in the former we list the important input parameters.

- M: the mass of the black hole;
- L_d: the luminosity of the accretion disk.
- R_diss: the distance from the black hole where the jet dissipates.
- P'_i: the power, calculated in the jet rest frame, injected into the source in the form of relativistic electrons.
- B: the magnetic field on the dissipation region;
- Γ_max: the value of bulk Lorentz factor after the acceleration phase, in which the bulk Lorentz factor increases as $[R/(3R_\mathrm{S})]^{1/2}$.
- θ_v: the viewing angle.
- γ_b: value of the random Lorentz factor at which the injected particle distribution $Q(\gamma)$ changes slope.
- γ_max: value of maximum random Lorentz factor of the injected electrons.
- s_2: slope of $Q(\gamma)$ above γ_b.

These amount to 10 parameters. If we use $\theta_\mathrm{v} \sim 1/\Gamma$, as discussed in §9, then the number of relevant parameters decreases to 9. Note that we do not consider P_j as an input parameter, since it

is derived once calculating the total electron energy density in the dissipation region, and assuming a given number of (cold) proton per emitting electron.

The following parameters are either unimportant or are well constrained:

- R_X: the extension of the X–ray corona. We fix it to $30R_\mathrm{S}$.
- R_out: the outer radius of the accretion disk. For the shown illustrative examples, we fixed it at 500 Schwarzschild radii, and we have shown that changing it has a modest influence on U'_d.
- s_1: slope of $Q(\gamma)$ below γ_b. It is bound to be very flat (i.e. $-1 < s_1 < 1$).
- α_X: the spectral shape of the coronal X–ray flux. We fix it to $\alpha_X = 1$.
- $h\nu_\mathrm{c}$: the high energy cut–off of the X–ray coronal flux. We fix it at 150 keV.
- L_X: total X–ray luminosity of the corona. We fix it to $L_X = 0.3L_\mathrm{d}$.
- f_BLR: fraction of L_d intercepted by the BLR and re–emitted in broad lines. We fix it to $f_\mathrm{BLR} = 0.1$
- $f_\mathrm{BLR,X}$: fraction of L_X of the corona scattered by the BLR. We fix it to $f_\mathrm{BLR,X} = 0.01$
- f_IR: fraction of L_d intercepted by the torus and re–emitted in IR. We fix it to $f_\mathrm{IR} = 0.5$.
- ψ: semi–aperture angle of the jet. We fix it to $\psi = 0.1$.
- U_star: this is the radiation energy density within the bulge of the host galaxy. We approximated it with the constant value $U_\mathrm{star} = 10^{-10}$ erg cm^{-3}.
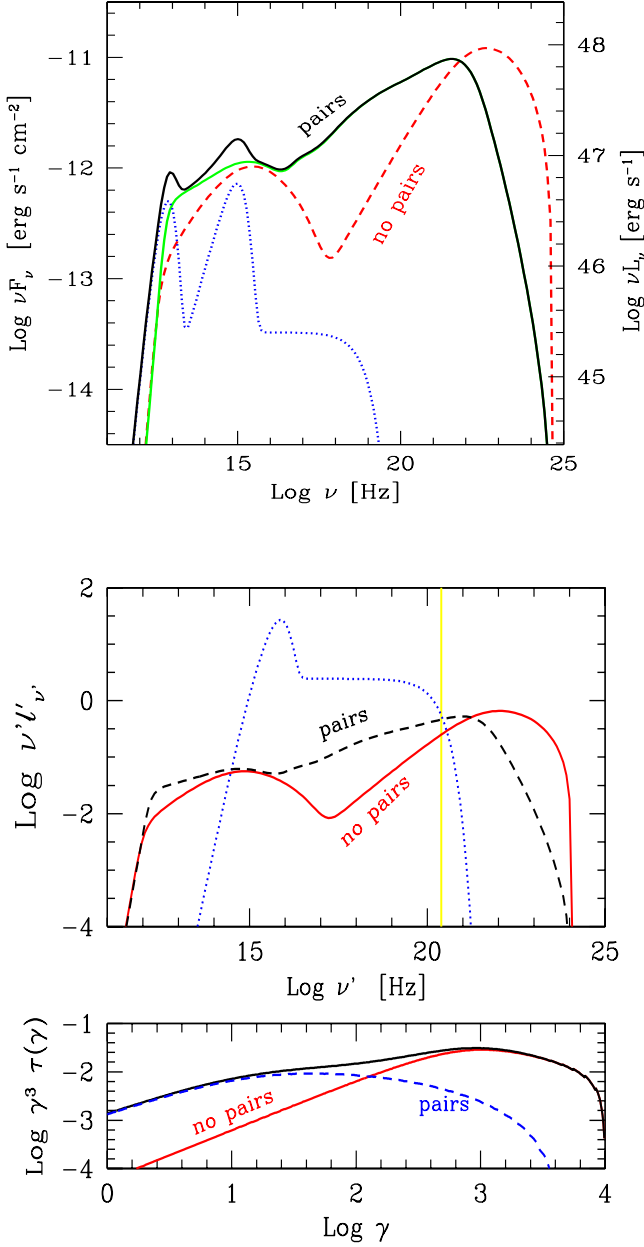
4 THE ROLE OF PAIRS

At large distances from the black hole, the density of the photon targets for the γ–$\gamma \to e^\pm$ process is small, with few pairs being produced inside the emitting region. At small distances, instead, the presence of the X–ray corona makes pairs easy to create. With our assumptions, we can see the effects of the reprocessing of the spectrum due to pairs. Whenever pairs are produced inside the emitting region at small R_diss, the radiative cooling rates are large, implying that all particles cool in one light crossing time. This in turn implies a particle distribution of the form given by Eq. 8, with $\gamma_\mathrm{cool} \sim 1$.

One necessary ingredient for making pairs important is the relative amount of power emitted above the energy threshold $m_e c^2$ (in the comoving frame). If this power is a small fraction of the total, the reprocessing will be modest, even if all the γ–rays get absorbed. There is then the possibility to have a large jet power dissipated close to the accretion disk, but with electrons of lower energies, whose emission is mostly below threshold. Furthermore, even if the electron energies are large, the bulk Lorentz factor could be small, especially very close to the accretion disk, where presumably the jet just starts to accelerate. In this case the magnetic energy density becomes more dominant with respect to the disk radiation, implying a relatively modest high energy emission, and furthermore the whole spectrum is much less boosted.

In the following we will consider the case of two jets with the same parameters, except that the first is moving with a large Γ already at small R_diss, the other, instead, is accelerating.
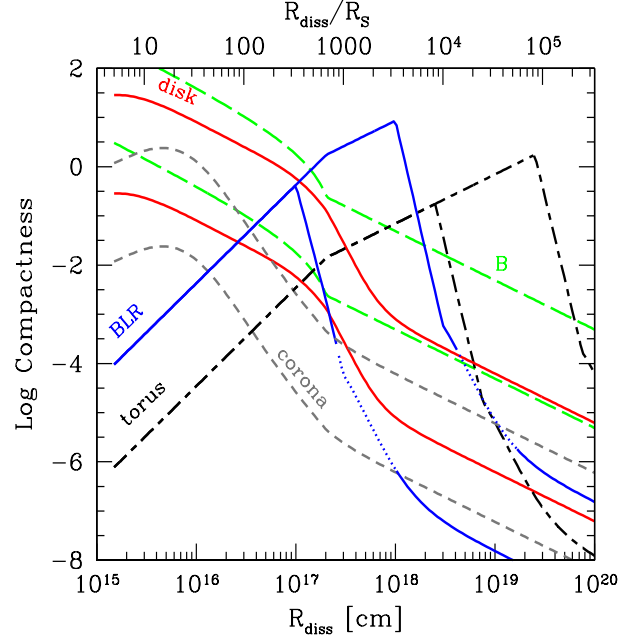
Consider Fig. 6: it shows the effects of including the γ–$\gamma \to e^\pm$ on the final spectrum. In the middle panel of Fig. 6 the same spectra are shown as seen in the comoving frame. In this case on the y–axis we plot the specific compactness, defined as $\ell'(\nu') \equiv \sigma_\mathrm{T} L'(\nu')/(r_\mathrm{diss} m_e c^3)$. The bottom panel of this figure shows the particle distribution (considering or not the produced

Figure 7. The compactness $\ell' \equiv 4\pi U' \sigma_T r_{\mathrm{diss}}/(m_e c^2)$ as measured in the comoving frame of a source of size r_{diss} as a function of R_{diss}. We use the same parameters used to construct the top panel of Fig. 2.

Figure 6. Top panel: example of how reprocessing due to electron–positron pairs can be important, if the dissipation region is located too close to the accretion disk and its X–ray corona, *and* if this region produces γ–rays above the pair–production threshold. The two humps at low energies correspond to the flux produced by the accretion disk and the IR flux from the torus. See Tab. 1 for the parameters used to construct the shown SED. Mid panel: the SED as observed in the comoving frame. Bottom panel: the particle distribution $\gamma^3 \tau(\gamma)$. For this example, the maximum particle Lorentz factor is $\gamma_{\mathrm{max}} = 10^4$ and $\gamma_b = 10^3$. A redshift $z = 3$ has been assumed.

pairs) in the form $\gamma^3 \tau(\gamma) \equiv \gamma^3 \sigma_T r_{\mathrm{diss}} N(\gamma)$. The γ^3 factor makes the $\gamma^3 \tau(\gamma)$ distribution to have a peak: electrons at this peak are the ones producing the peaks in the νL_ν synchrotron and inverse Compton spectra. The parameters used for this example are listed in Tab. 1.

One can see that pairs redistribute the power from high to low frequencies. The $N(\gamma)$ distribution steepens at low energies

(where pairs contribute the most), and this softens the emitted spectrum especially in the X–ray range. The reprocessing of the X–ray spectrum is stronger than at lower frequencies because the low energy electrons emit, by synchrotron, self absorbed radiation, whose shape and normalisation are largely independent of the slope of $N(\gamma)$. Instead, in the X–ray range, the presence of the intense optical–UV radiation field coming from the accretion disk implies that the dominant process is the external Compton (EC) scattering with these photons. In turn, this implies that the radiation we see in the soft and hard X–ray range is due to relatively low energy electrons. In fact, the scattered frequency $\nu \sim \gamma^2 \Gamma^2 \nu_0$, where ν_0 is the (observed) frequency of the seed photon. Therefore, at 10 keV, we are observing the radiation produced by electrons with $\gamma \sim 50 \, \nu_{0,15}^{-1/2} \Gamma^{-1} \sim$ a few.

In the above example we have, on purpose, assumed that the dissipation region, although very close to the black hole, is already moving at large speeds, corresponding to a bulk Lorentz factor of 10. We may ask, instead, what happens if the same kind of dissipation occurs while the jet is still accelerating, and has therefore a relatively small bulk velocity when it is close to the black hole.

To this aim, Fig. 7 shows the compactness ℓ', as measured in the comoving frame, as a function of R_{diss}, for an accelerating jet. We define this comoving compactness as:

$$\ell' \equiv \frac{4\pi U' \sigma_T r_{\mathrm{diss}}}{m_e c^2} \qquad (27)$$

where r_{diss} is the size of the blob. The term U' is the external radiation energy densities. The compactness is directly associated to the optical depth of the $\gamma-\gamma \rightarrow e^{\pm}$ process, and it describes the absorption probability of a γ–ray photon while it is inside the blob. In other words, this definition does not account for the absorption a photon can suffer while it has already escaped the blob. It also neglects the contribution of the internal radiation energy density due to the synchrotron and the synchrotron self Compton (SSC) emis-

sion. Fig. 7 shows that there are three distances where the compactness is large:

(i) At the base of the jet the main targets for the γ–γ process are the X–ray photons produced by the corona. They can interact with γ–ray photons just above threshold, implying that the absorption is important. However, at these distances, the magnetic energy density is larger than the external radiation energy density (dominated by the disk radiation), and this implies a modest external Compton scattering, and a modest production of γ–rays.

(ii) The compactness becomes large again for $R_{\rm diss} \sim R_{\rm BLR}$. Since the main contribution to U' is due to the BLR photons, (seen at UV frequencies in the comoving frame), the absorbed γ–rays will have GeV energies (see next subsection for more details).

(iii) The third relevant range of distances corresponds to $R_{\rm diss} \sim R_{\rm IR}$. The main targets for the absorption process are the IR photons produces by the torus, absorbing TeV γ–rays.

Fig. 8 shows three SED corresponding to $R_{\rm diss} = 10$, 100 and $10^3 R_{\rm S}$, with an electron injection function equal to the one used in Fig. 6, but assuming $\Gamma = \min[15, (R_{\rm diss}/3R_{\rm S})^{1/2}]$. Tab. 1 lists the parameters. We can see the dramatic changes with respect to Fig. 6, and also among the three shown models. Pair production, although present (compare solid and dashed lines), is marginal and there is no noticeable reprocessing of the primary spectrum. This is due to the much reduced importance of the external radiation when Γ is small. As a consequence, the spectrum is dominated by the synchrotron emission, with a small fraction of the power being emitted above the pair production energy threshold. This in turn implies that early (i.e. close to the black hole) dissipation is not an efficient mechanism to produce electron–positron pairs. Since a small Γ means small Doppler boosting, the produced spectra at small distances are undetectable, overwhelmed by the emission of more distant and fastly moving components.

When Γ is large, therefore for the $R_{\rm diss} = 10^3 R_{\rm S}$ case, the relevant absorbing photons are those of the broad line region, with a very modest contribution from the coronal X–rays reflected by the BLR material. The overall effect is marginal.

We can conclude that a "canonical" jet can dissipate part of its kinetic energy even at small distances. One way to avoid strong pair production is to have small electron energies, emitting a small power above the pair production threshold. Alternatively, if the jet is accelerating, and close to the black hole it has a modest Γ–factor, the produced radiation is hardly observable because the Doppler boost is limited. In relative terms, the synchrotron luminosity should be dominant, with a small fraction of power being emitted at high energies.

4.1 Pair production versus Klein–Nishina effects

In powerful blazars, the high energy flux, at $\sim$GeV energies, is dominated by the inverse Compton process between high energy electrons and external radiation. In Tavecchio & Ghisellini (2008) we pointed out that when the dominant contribution to the seed photon for scattering is given by the BLR, the hydrogen Lyman–α photons are the most prominent ones. The fact that there is a characteristic frequency of the seed photons allows to easily calculate when the Klein–Nishina effects (decrease of the scattering cross section with energy) are important. For completeness, we briefly repeat here the argument, with the aim to extend it to cases in which $R_{\rm diss}$ is beyond the BLR, and as a consequence, the relevant seed photons becomes the IR ones.

In the comoving frame, and as long as we are within the
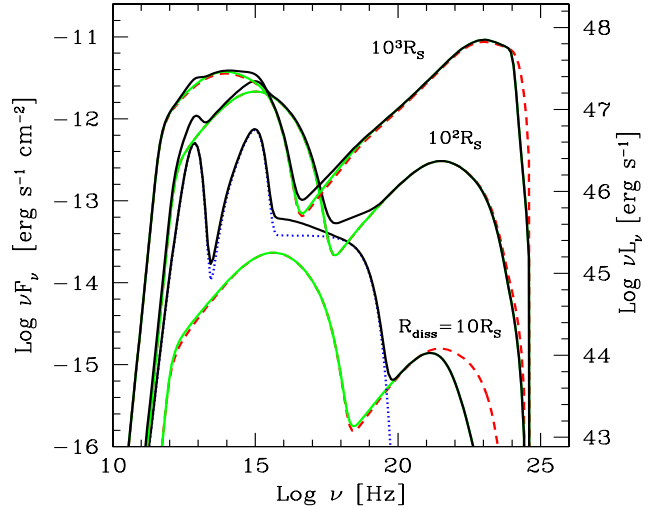
Figure 8. Same as Fig. 6, but for an accelerating jet and for different $R_{\rm diss}$. In this case, in the comoving frame of the jet, the magnetic energy density is dominant for $R_{\rm diss} = 10$ and $100R_{\rm S}$. Furthermore, the much reduced Doppler boosting for small values of $R_{\rm diss}$ implies a very small received flux. There is some γ–γ absorption (compare solid and dashed lines, the latter corresponding to switching off the γ–γ process), but involving a very small amount of power. Consequently, pairs reprocessing is unimportant. Light grey lines (green in the electronic version) correspond to the non–thermal spectrum, black lines include the contribution from the accretion disk, its X–ray corona and the emission from the IR torus.

BLR, The observed seed Lyman–α frequency is observed at $\nu'_{\rm L\alpha} = 2\Gamma\nu_{\rm L\alpha}$. To be in the Thomson scattering regime we require that

$$2\Gamma h\nu_{\rm L\alpha} < \frac{m_{\rm e}c^2}{\gamma} \qquad (28)$$

If the random Lorentz factor γ of the electron satisfies this condition, the energy of the scattered photon is

$$\nu_{\rm KN} = \frac{4}{3}\gamma^2\nu_{\rm L\alpha}\frac{2\Gamma\delta}{1+z} = 15\frac{\delta}{\Gamma(1+z)} \ {\rm GeV} \qquad (29)$$

Above this energy, the spectrum steepens due to the decreased efficiency of the scattering process. This may well mimic the effect of photon–photon absorption, making it difficult to discriminate between the two effects. Consider also that the Lyman–α photons are the best targets for the photon–photon process at these energies and in these conditions (namely, relatively far from the accretion disk, but still within the BLR).

We can repeat the very same argument assuming that the relevant seed photons are the ones produced by the IR torus. This occurs when the dissipation region is beyond the BLR but within $R_{\rm IR}$. In this case the relevant frequency is $\nu_{\rm IR} = 3 \times 10^{13}$ Hz and we can rewrite Eq. 29 as

$$\nu_{\rm KN} = \frac{4}{3}\gamma^2\nu_{\rm IR}\frac{2\Gamma\delta}{1+z} = 1.2\frac{\delta}{\Gamma(1+z)} \ {\rm TeV} \qquad (30)$$

This implies that, if we do see a spectrum which is unbroken even above $15/(1+z)$ GeV, we can conclude that the dissipation region is beyond the BLR.

Also in this case, the "intrinsic" absorption due to the γ–γ process is expected to become important at $\sim \nu_{\rm KN}$. There is therefore a range, between $15/(1+z)$ and $\sim 1000/(1+z)$ GeV, in which the intrinsic spectrum should not suffer from the Klein–Nishina nor from the γ–γ process due to "internal" absorption. These sources

are thus the best candidates for studying the photon–photon absorption due to the cosmic optical–UV background radiation.

5   DISSIPATION AT LARGE DISTANCES

Although there are strong indications that *most* of the observed radiation originates in a well localised region of the jet, there is also compelling evidence that the jet dissipates also in other regions, larger and more distant from its base. In fact, in the radio band, we do see bright knots at different distances contributing to form the characteristic flat total radio spectrum of the entire jet, and we do observed optical and X–ray knots also at hundreds of kpc from the jet apex. The power associated to these, often resolved, features is a small fraction of the total observed jet bolometric luminosity, but in specific bands the flux produced at larger distances can be comparable to the flux produced in the most active region.

It is therefore instructive to calculate the predicted spectrum as a function of distance, extending our analysis well beyond the region of influence of the IR flux produced by the torus, and therefore analysing the effects of the radiation energy density of the cosmic background radiation (CMB). This has already been pointed out as an important source of seed photons for enhancing the inverse Compton flux of the bright X–ray knots detected by the Chandra satellite at tens and hundreds of kpc from the core of the jet (Tavecchio et al. 2000; Celotti Ghisellini & Chiaberge 2001).

Fig. 9 shows the different contributions to the radiation energy densities as seen in the comoving frame, compared to $U'_{\rm B}$, and including $U'_{\rm CMB}$, important for large distances. To construct this figure we have assumed $M = 10^9 M_\odot$, $L_{\rm d} = 10^{47}$erg s^{-1}, $P'_{\rm i} = 10^{44}$ erg s^{-1}, $P_{\rm B} = 10^{46}$ erg s^{-1}, $z = 3$ and $\Gamma = \min[15, (R_{\rm diss}/3R_{\rm S})^{1/2}]$. This figures shows that $U'_{\rm B}$ dominates only in two regions of the jet: in the vicinity of the black hole and at $R_{\rm diss} \sim 10^{20}$–$10^{21}$ cm. Within these two distances, $U'_{\rm BLR}$ and $U'_{\rm IR}$ dominate, and beyond 10^{21} cm $U'_{\rm CMB}$ takes over. This has two important and immediate consequences:

(i) The external Compton radiation will be more important than the synchrotron (and the SSC, if $y \sim 1$) radiation at all distances, except the (relatively narrow) distance intervals where $U'_{\rm B}$ dominates.

(ii) At large distances the jet is conical, and the blob size scales linearly with $R_{\rm diss}$ (namely the jet is a cone with the same aperture angle ψ). Then the light crossing time $t_{\rm cross} = \psi R_{\rm diss}/c$. This hypothesis means that $\gamma_{\rm cool}$ reaches a maximum where $U'_{\rm B} = U'_{\rm CMB}$.

To understand the second issue, consider the value of $\gamma_{\rm cool}$ after a time $t_{\rm cross}$.

$$\gamma_{\rm cool} = \frac{3m_{\rm e}c^2}{4\sigma_{\rm T}r_{\rm diss}U'} \tag{31}$$

In the regions of interest (i.e. above 1 kpc), $U'_{\rm CMB}$ is constant, while $U'_{\rm B} \propto r_{\rm diss}^{-2}$. Therefore the maximum $\gamma_{\rm cool}$ occur when $U'_{\rm CMB} = U'_{\rm B}$, i.e. at

$$\psi R_{\rm eq} = \left[\frac{P_{\rm B}}{\pi ac}\right]^{1/2} \frac{1}{T_0^2(1+z)^2\Gamma^2} \tag{32}$$

Inserting this in Eq. 31 and setting $U' = U'_{\rm CMB} + U'_{\rm B} = 2U'_{\rm CMB}$,

we obtain:

$$
\begin{aligned}
\gamma_{\rm cool}^{\rm max} &= \frac{3m_{\rm e}c^2}{4\sigma_{\rm T}T_0^2(1+z)^2}\left(\frac{\pi c}{aP_{\rm B}}\right)^{1/2} \\
&= \frac{3.08\times10^6}{(1+z)^2 P_{\rm B,46}^{1/2}}
\end{aligned} \tag{33}
$$

Independent of Γ. Electrons with this energy emit an observed synchrotron frequency $\nu_{\rm cool}$ given by:

$$
\begin{aligned}
\nu_{\rm cool}^{\rm syn} &\sim 3.6\times10^6 B\gamma_{\rm cool}^2\delta \\
&= 1.09\times10^{14}\frac{\Gamma\delta}{(1+z)^3 L_{\rm B,46}} \quad {\rm Hz}
\end{aligned} \tag{34}
$$

Analogously, the observed frequency emitted by these electrons scattering the peak of the CMB radiation is

$$
\begin{aligned}
\nu_{\rm cool}^{\rm IC} &\sim \frac{4}{3}\frac{3.93kT_0}{h}\gamma_{\rm cool}^2\Gamma\delta \\
&= 2.8\times10^{24}\frac{\Gamma\delta}{(1+z)^4 P_{\rm B,46}} \quad {\rm Hz}
\end{aligned} \tag{35}
$$

We thus expect that the synchrotron spectrum produced in powerful jets, at large distances, cuts–off at a frequency given by Eq. 34, or somewhat larger if, at these scales, the active region has a size smaller than ψR (implying a smaller cooling time, and thus electron energies greater than the ones given by Eq. 33).

Fig. 10 shows the predicted SEDs corresponding to different $R_{\rm diss}$ (indicated by the vertical grey lines in Fig. 9 with the corresponding numbers); all the relevant input parameters for the different SEDs are reported in Tab. 1. The profile of the external radiation and the value of the magnetic field correspond to what shown in Fig. 9. We have also assumed that, increasing $R_{\rm diss}$, the injected power in relativistic electrons decreases by a factor 3 increasing $R_{\rm diss}$ by a factor 10. At the same time, we assumed that the maximum energy of the injected electrons increases by a factor 3 for a tenfold increase of $R_{\rm diss}$. These choices are arbitrary, but reflect the observational evidence that the bolometric radiative output of jets decreases with distance. Furthermore the existence of optical jets, whose emission is due to the synchrotron process, ensures that at large jet scales there are very energetic electrons.

The first three SEDs (number 1, 2 and 3, corresponding to $R_{\rm diss} = 10^3$, 10^4 and $10^5 R_{\rm S}$, respectively) have a large Compton dominance, corresponding to the large ratio between the external radiation and the magnetic energy densities. Note that only the first uses the BLR photons as the main seeds for the Compton process (and thus it has the largest peak frequency), while the SED 2 and SED 3 use the IR photons as seeds. SED 1 is dominating in the γ–ray band (above $\sim$1 MeV), while in the far IR to UV bands there is the contribution of the thermal radiation (accretion disk and IR torus). Remarkably, the soft X–rays are produced almost equally by these three jet dissipation sites (see also below).

SED 4 (i.e. $R_{\rm diss} = 10^6 R_{\rm S}$) is the only one where the magnetic energy density dominates. Correspondingly, the synchrotron flux dominates the bolometric output. Comparing SED 3 and SED 4, we note that they have total luminosities that differ by more than a factor 3. This is due to the incomplete electron cooling, and implies that not all the power injected in random energy of the electrons can be radiated in one crossing time. For the same reason, there is a rather large jump in $\gamma_{\rm cool}$ between $R_{\rm diss} = 10^5$ and $10^6 R_{\rm S}$ (see the bottom panel of Fig. 9), corresponding to the fast drop of the energy density of the external radiation between these two distances.

SED 5 ($R_{\rm diss} = 10^7 R_{\rm S}$, or 1 kpc) has again a relatively large
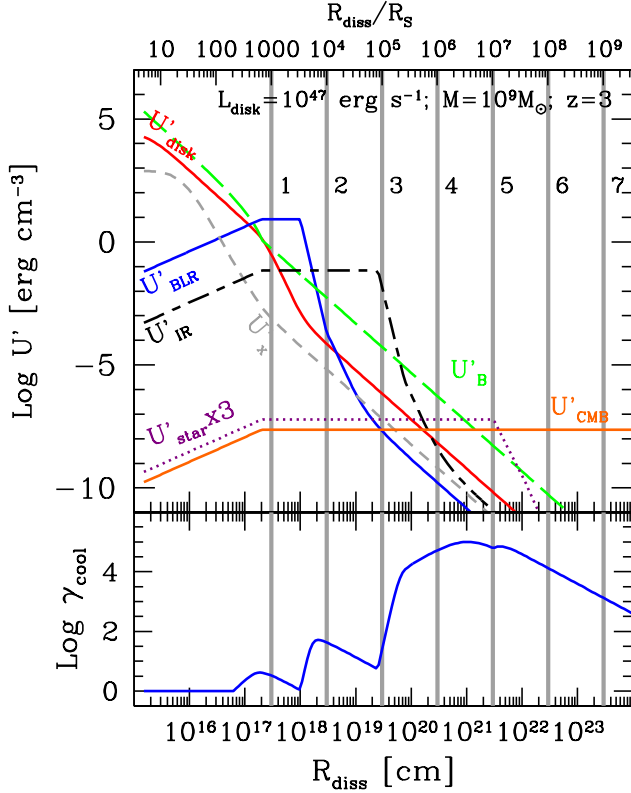
Figure 9. Top panel: the contributions to the radiation energy density as seen in the comoving frame of the emitting blob, as labelled, and the magnetic energy density as a function of the distance of the blob to the black hole. We assumed: $M = 10^9 M_\odot$, $L_d = 10^{47}$ erg s^{-1}, $z = 3$ and $\Gamma = \min[15, (R_{\rm diss}/3R_S)^{1/2}]$. The Poynting flux is $P_B = 10^{46}$ erg s^{-1} once the jet has reached its maximum bulk Lorentz factor. The grey vertical lines indicates the distances assumed to construct the SEDs in Fig. 10, the different numbers help to identify the corresponding SED. The bottom bottom panel shows $\gamma_{\rm cool}$ (after one light crossing time since the start of the injection) as a function of $R_{\rm diss}$.

Compton dominance, due to the prevailing of the CMB and the starlight (from the galaxy bulge) energy densities over the magnetic one. This SED has almost the largest possible $\gamma_{\rm cool}$ (see Fig. 9) and this is reflected in the calculated SED, having the largest peak frequency of the high energy component.

SED 6 and 7 ($R_{\rm diss} = 10^8$ and $10^9 R_S$, or 10 and 100 kpc, respectively) have a very large Compton dominance, due to the fact that $U'_{\rm CMB}$ is constant, while U'_B decreases with distance. As discussed previously, the constancy of $U'_{\rm CMB}$ makes $\gamma_{\rm cool}$ to decrease with $R_{\rm diss}$, since the cooling time at which $\gamma_{\rm cool}$ is calculated increases. This also implies that, despite the decrease of P'_i, the SED 5, 6 and 7 have the same bolometric luminosity, because a larger portion of the electron population can cool in one $t_{\rm cross}$.

The sum of all SEDs is shown by the black thick line in Fig. 10. Note that, in the radio band, the total flux $F_\nu \propto \nu^0$ (or slightly harder), as observed. At frequencies greater than the radio ones, the total flux is dominated by SED 1, but the flux originating at relatively large scales can be important in some frequency bands, as the soft X–ray one, with important consequences on the observed variability and the correlation of variability in different bands. According to Fig. 10 (which is, we re–iterate, only one possible example, shown for illustration) the correlation between the γ–ray and
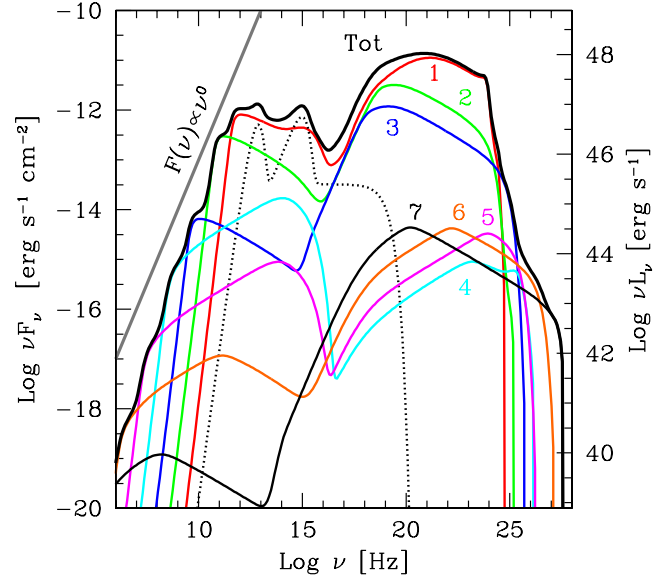
Figure 10. Sequence of SEDs calculated for different $R_{\rm diss}$ from $10^3 R_S$ to $10^9 R_S$ (one per decade). The injected electron luminosity is $P'_i = 10^{44}$ erg s^{-1} for $R_{\rm diss} = 10^3 R_S$ and is reduced by a factor 3 each decade. The particle distribution has always the same $\gamma_b = 100$, while $\gamma_{\rm max}$ increases by a factor 3 each decade starting from $\gamma_{\rm max} = 10^4$ for $R_{\rm diss} = 10^3 R_S$. All other parameters are the same as in Fig. 9. What shown are the observed spectra neglecting the absorption of the high energy flux due to the IR–opt–UV cosmic background. The numbers correspond to the same numbers in Fig. 9 and correspond to the SED at different $R_{\rm diss}$. The thicker black line is the sum of all the SED. The grey line at radio frequencies indicates $F(\nu) \propto \nu^0$. The received flux is calculated assuming that the source is at $z = 3$.

the IR flux should be tighter than the correlation between the γ–ray and the soft X–ray flux, diluted by the the flux originating at larger scales (that can vary on longer timescales). Furthermore, if the soft X–ray flux is produced by external Compton, the energies of the electron emitting it are relatively modest (namely $\gamma \sim 1$–10) while, in the γ–ray band, we see the emission of the electrons with the highest energies (which emit, by synchrotron, at IR–optical frequencies). The cooling timescales are therefore different, producing different variability if $t_{\rm cool}$ at low energies is longer than the light crossing time. If not, then we expect the same variability pattern for emission produced in the same zone. One example of different variability behaviour is displayed by the blazar 3C 454.3, as recently studied by Bonning et al. (2008), and has been interpreted by these authors as a consequence of the different energies of the electron contributing in the X–ray and γ–ray bands. The contribution to the X–ray flux by other zones of the jet can be an alternative possibility.

6 CHANGING THE BLACK HOLE MASS

It is instructive to study the SED produced by the jet in FSRQs of different black hole masses, scaling the relevant quantities with the Schwarzschild radius and the Eddington luminosity. To this aim we show in Fig. 11 a sequence of SED with the black hole mass ranging from 3×10^7 to $3 \times 10^9 M_\odot$. We assume that $R_{\rm diss}$ is always at 500 Schwarzschild radii and that $L_d = 0.067 L_{\rm Edd}$, with a corona with an X–ray luminosity equal to one third that of the

Fig. [1]	$R_{\rm diss}$ [2]	M [3]	$R_{\rm BLR}$ [4]	$P'_{\rm i}$ [5]	$L_{\rm d}$ [6]	B [7]	Γ [8]	$\theta_{\rm v}$ [9]	$\gamma_{\rm b}$ [10]	$\gamma_{\rm max}$ [11]	s_1 [12]	s_2 [13]	z [14]	Notes [15]
6	6 (20)	1e9	1e3	0.1	100 (0.67)	200	10	3	1e3	1e4	0	2.5	3	Pairs–no pairs
8	3 (10)	1e9	1e3	0.1	100 (0.67)	1.6e3	1.8	3	1e3	1e4	0	2.5	3	Pairs–no pairs
8	30 (100)	1e9	1e3	0.1	100 (0.67)	120	5.8	3	1e3	1e4	0	2.5	3	Pairs–no pairs
8	300 (1e3)	1e9	1e3	0.1	100 (0.67)	5.6	10	3	1e3	1e4	0	2.5	3	Pairs–no pairs
10	3e2 (1e3)	1e9	1e3	7.3e–2	100 (0.67)	3.6	15	3	100	1e4	1	2.5	3	$R_{\rm diss}$ seq.
10	3e3 (1e4)	1e9	1e3	2.4e–2	100 (0.67)	0.36	15	3	100	3e4	1	2.5	3	$R_{\rm diss}$ seq.
10	3e4 (1e5)	1e9	1e3	8.1e–3	100 (0.67)	3.6e–2	15	3	100	9e4	1	2.5	3	$R_{\rm diss}$ seq.
10	3e5 (1e6)	1e9	1e3	2.7e–3	100 (0.67)	3.6e–3	15	3	100	2.7e5	1	2.5	3	$R_{\rm diss}$ seq.
10	3e6 (1e7)	1e9	1e3	9e–4	100 (0.67)	3.6e–4	15	3	100	8.1e5	1	2.5	3	$R_{\rm diss}$ seq.
10	3e7 (1e8)	1e9	1e3	3e–4	100 (0.67)	3.6e–5	15	3	100	2.4e6	1	2.5	3	$R_{\rm diss}$ seq.
10	3e8 (1e9)	1e9	1e3	1e–4	100 (0.67)	3.6e–6	15	3	100	7.3e6	1	2.5	3	$R_{\rm diss}$ seq.
11	4.5 (500)	3e7	55	3e–3	0.3 (0.067)	13.3	15	3	100	1e4	1	2.5	3	M seq.
11	15 (500)	1e8	100	0.01	1 (0.067)	7.3	15	3	100	1e4	1	2.5	3	M seq.
11	45 (500)	3e8	173	0.03	3 (0.067)	4.2	15	3	100	1e4	1	2.5	3	M seq.
11	150 (500)	1e9	317	0.1	10 (0.067)	2.3	15	3	100	1e4	1	2.5	3	M seq.
11	450 (500)	3e9	549	0.3	30 (0.067)	1.3	15	3	100	1e4	1	2.5	3	M seq.
12: 3C 279	114 (380)	1e9	173	0.06	3 (0.02)	3.1	11.3	3	250	4e3	1	2.2	0.536	high EGRET
12: 3C 279	300 (1e3)	1e9	173	0.04	3 (0.02)	0.42	16	3	3e3	3e5	0	2.7	0.536	TeV
12: 3C 279	72 (240)	1e9	173	9e–3	3 (0.02)	7.7	8.9	3	160	1.2e3	0	2.7	0.536	low EGRET
13: 1428	680 (1.5e3)	1.5e9	1.2e3	0.1	135 (0.6)	1.2	15	2.5	30	3e3	0	2.4	4.72	*Beppo*SAX
13: 1428	6.8e3 (1.5e4)	1.5e9	1.2e3	0.1	135 (0.6)	0.12	15	2.5	30	3e3	0	2.4	4.72	$R_{\rm diss} \times 10$
13: 1428	68 (150)	1.5e9	1.2e3	0.1	135 (0.6)	44	7.1	2.5	30	3e3	0	2.4	4.72	$R_{\rm diss} \times 0.1$
14: 2149	960 (800)	4e9	1.2e3	0.1	150 (0.25)	1.7	12	3	10	1e3	–1	2.6	2.345	*Swift* data
14: 2149	9.6e3 (8e3)	4e9	1.2e3	0.1	150 (0.25)	0.17	12	3	10	1e3	–1	2.6	2.345	$R_{\rm diss} \times 10$
14: 2149	96 (80)	4e9	1.2e3	0.1	150 (0.25)	43	5.2	3	10	1e3	–1	2.6	2.345	$R_{\rm diss} \times 0.1$
15	810 (900)	3e9	1.7e3	0.4	302 (0.67)	2.4	13	3	100	3e3	0	2.5	—	Blazar seq.
15	810 (900)	3e9	636	0.04	41 (0.09)	0.9	13	3	200	3e4	0	2.5	—	Blazar seq.
15	120 (400)	1e9	387	4e–3	15 (0.1)	5.5	11.5	3	200	1.5e4	0	2.5	—	Blazar seq.
15	210 (700)	1e9	—	1e–3	—	0.2	15	3	600	2e5	0	2.5	—	Blazar seq.
15	210 (700)	1e9	—	5e–4	—	0.1	15	3	3e3	7e5	0	2.5	—	Blazar seq.

Table 1. List of parameters used to construct the SED shown in Figg. 6–13. Col. [1]: figure number where the model is shown; Col. [2]: dissipation radius in units of 10^{15} cm and (in parenthesis) in units of $R_{\rm S}$; Col. [3]: black hole mass in solar masses; Col. [4]: size of the BLR in units of 10^{15} cm; Col. [5]: power injected in the blob calculated in the comoving frame, in units of 10^{45} erg s^{-1}; Col. [6]: accretion disk luminosity in units of 10^{45} erg s^{-1} and (in parenthesis) in units of $L_{\rm Edd}$; Col. [7]: magnetic field in Gauss; Col. [8]: bulk Lorentz factor at $R_{\rm diss}$; Col. [9]: viewing angle in degrees; Col. [10] and [11]: break and maximum random Lorentz factors of the injected electrons; Col. [12] and [13]: slopes of the injected electron distribution [$Q(\gamma)$] below and above $\gamma_{\rm b}$; Col. [14]: redshift; Col. [15]: some notes. For all cases the X–ray corona luminosity $L_X = 0.3L_{\rm d}$. Its spectral shape is assumed to be $\propto \nu^{-1} \exp(-h\nu/150\,{\rm keV})$.

disk. We assume that the power in relativistic electrons injected into the dissipation region of the jet scales with the black hole mass as $P'_{\rm i} = 10^{44} M_9$ erg s^{-1}. Electrons are injected between $\gamma_1 = 10^2$ and $\gamma_2 = 10^4$ in all cases. The bulk Lorentz factor is $\Gamma = 15$ for all cases and the redshift is $z = 3$. At the assumed $R_{\rm diss}$ the jet has already reached its maximum Γ, and at these distances the Poynting flux is assumed to scale as $P_{\rm B} = 6.7 \times 10^{-3} L_{\rm Edd}$. We then have

$$U_{\rm B} \propto \frac{L_{\rm Edd}}{\Gamma^2 R_{\rm diss}^2} \propto \frac{M}{M^2} \propto \frac{1}{M} \qquad (36)$$

which follows from the assumption of $R_{\rm diss}/R_{\rm S}$ =const and Γ =const. For all our cases, the dissipation occurs within the BLR, which yields a constant radiation energy density $U'_{\rm BLR}$ since Γ is the same. As a consequence, the ratio $L_{\rm EC}/L_{\rm syn} \sim U'_{\rm BLR}/U_{\rm B} \propto M$. This is the reason of the increasing dominance of the inverse Compton emission increasing the black hole mass. This implies that blazars with large black hole masses should preferentially be more Compton dominated, and therefore more easily detected by the Fermi satellite. In fact, in Fig. 11 one can see the 5σ sensitivity

of Fermi for 1 year of operation (grey line), suggesting that, at high redshifts, the detected blazars will preferentially have large black hole masses.

The importance of the EC relative to the SSC emission increases with the black hole mass, hardening the X–ray spectral shape. The SSC and EC components are shown separately for the SED corresponding to $M = 3 \times 10^7 M_\odot$, to illustrate the importance of the SSC flux. For larger masses the SSC components becomes relatively less important than the EC one. For the SED with $M = 3 \times 10^9 M_\odot$ we show the effects of neglecting the γ–γ absorption and the consequent reprocessing (dashed line). One can see that the primary (i.e. neglecting pairs) spectrum as a rather sharp cut–off due to the Klein–Nishina limit given by Eq. 29.
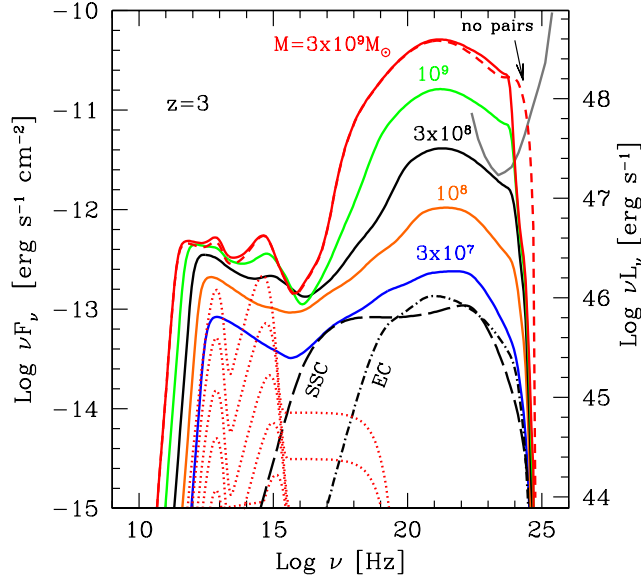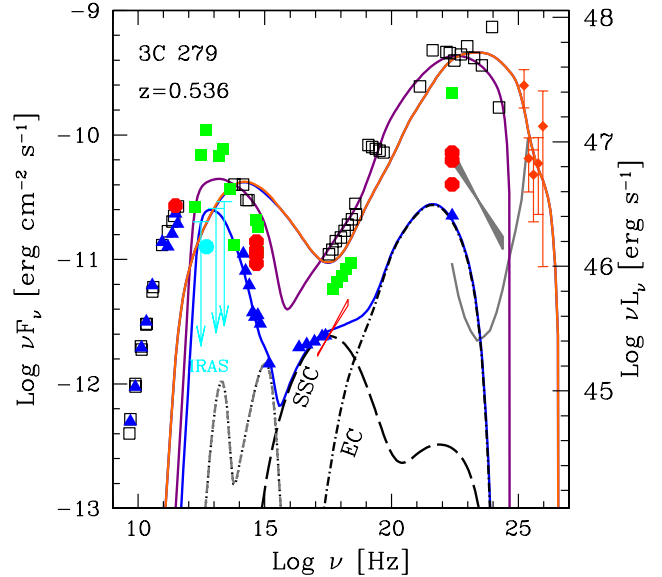
Figure 11. The observed SED for different black hole masses (from 3×10^7 to $3 \times 10^9 M_\odot$, as labelled) assuming that the dissipation takes place at $500 R_S$, that the accretion disk luminosity is $L_d = 0.067 L_{Edd}$, and that the power injected in the jet dissipation region scales as $P'_i = 10^{44} M_9$ erg s^{-1}. The bulk Lorentz factor is kept fixed at $\Gamma = 15$. The particles are always injected between $\gamma_1 = 10^2$ and $\gamma_2 = 10^4$. The grey line is the 5σ detection sensitivity of Fermi, after 1 year of operation. For the $M = 3 \times 10^7 M_\odot$ case we show, besides the total spectrum, the SSC and the EC components separately. This illustrates the importance of the SSC process for low values of the black hole masses. The dashed line (for the case with $M = 3 \times 10^9 M_\odot$) shows the spectrum neglecting photon–photon absorption and pair reprocessing. The received flux is calculated assuming that all sources are at $z = 3$.

Figure 12. SED of 3C 279 in different states together with the corresponding models, whose input parameters are listed in Tab. 1. See Ballo et al. (2002) and references therein for the sources of data points. Note that the high energy data–points (above 100 GeV) have been de–absorbed according to the Primack, Bullock & Somerville (2005) model used in Tavecchio & Mazin (2009). According to Eq. 30, the flux at these energies can be produced at relatively large distances from the black hole, beyond the BLR. In this case the main contribution to the seed photons is coming from the IR torus (solid light grey line, orange in the electronic version). In the low state (blue triangles) the SSC process is dominating the 2–10 keV X–ray flux. For this state only we show the SSC (long dashed line) and the EC flux (dot–dashed line) separately.

7 SOME ILLUSTRATIVE EXAMPLES

7.1 TeV FSRQs: the case of 3C 279

3C 279 has been recently detected in the TeV band (Albert et al. 2008), although its redshift, $z = 0.536$, implies a strong absorption of high energy γ–rays by the IR cosmic background. This demonstrates that also powerful blazars emit at large energies, up to the TeV band, even if the peak of their high energy hump may lye in the MeV–GeV band. Besides the consequences that this result has on the cosmic background, discussed in Sitarek & Bednarek (2008); Tavecchio & Mazin (2009); Liu, Bai & Ma (2008), we would like to discuss here another consequence, which concerns the primary spectrum of the source.

We have discussed previously that if the bulk of the inverse Compton spectrum uses BLR photons as seeds, then we expect a steepening of the intrinsic spectrum at $\sim 15/(1 + z) \sim 10$ GeV due to Klein–Nishina effects. This is shown in Fig. 12 as the darker line passing through an archival EGRET spectrum of the source (squares). For this model, in fact, the dissipation region is within the BLR, which is then giving most of the seed photons used for the scattering (see Tab. 1 for the all the input parameters). The rather abrupt cut–off seen at $\sim 2.5 \times 10^{24}$ Hz ~ 10 GeV is due this effect, and not to γ–γ internal absorption, which, in this particular example, is unnoticeable. To produce photons of larger energies and evade the Klein–Nishina limit we are forced to locate R_{diss} beyond the BLR, and then use the IR photons produced by the torus.

This is what the model does (lighter grey line, orange in the electronic version).

Note that the presence of a very high energy component in 3C 279 was predicted (before detection) by Błazejowski et al. (2000), who included the presence of a IR emitting torus (see their Fig. 4). The main difference of our modelling with respect to Błazejowski et al. (2000) is in the assumed temperature of the torus, assumed to be larger in that paper, implying a smaller size and an enhanced U'_{IR}.

If the jet of 3C 279 is "canonical" in the sense described in this paper, then a larger R_{diss} means a smaller magnetic field, and a larger bulk Lorentz factor (if it has not yet reached its maximum value). Then, according to these ideas, we show the entire modelled SED to compare it with the "high EGRET state" (squares) and the "low EGRET state" (triangles). For the latter model we have assumed a smaller R_{diss} and P'_i. This implies a small bulk Lorentz factor (hence a decreased importance of the external seed photons) and a large magnetic field, resulting in a SED of equal synchrotron and inverse Compton power.

3C 279 is one of the best studied γ–ray blazars, partly because it was very active during the observations of EGRET. It should not be taken, however, as the prototypical high power FSRQ, since its disk emission is very modest, as also directly suggested by its SED in the low state (Pian et al. 1999; see the triangles in Fig. 12, see Ballo et al. 2002 and references therein for the data): for our models we have assumed a black hole mass $M = 10^9 M_\odot$ and $L_d = 0.02 L_{Edd}$. It is therefore instructive to show example
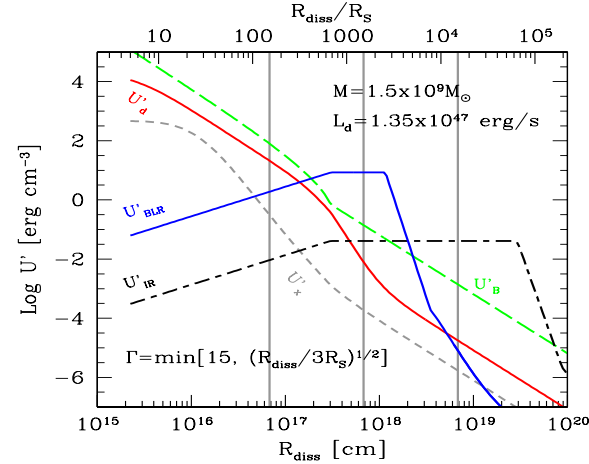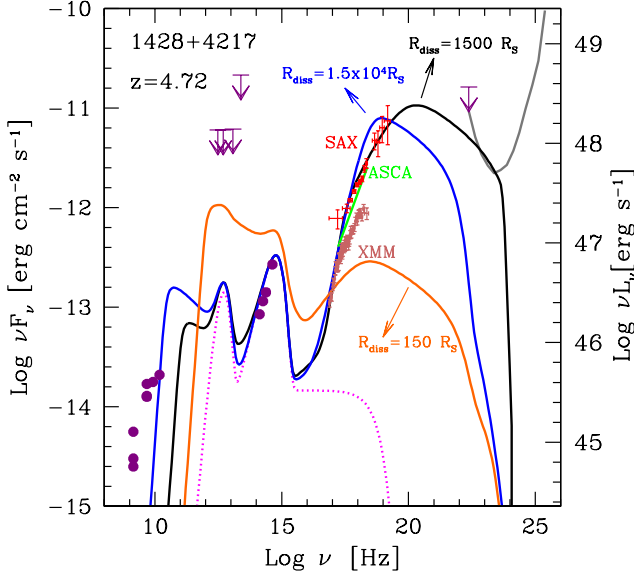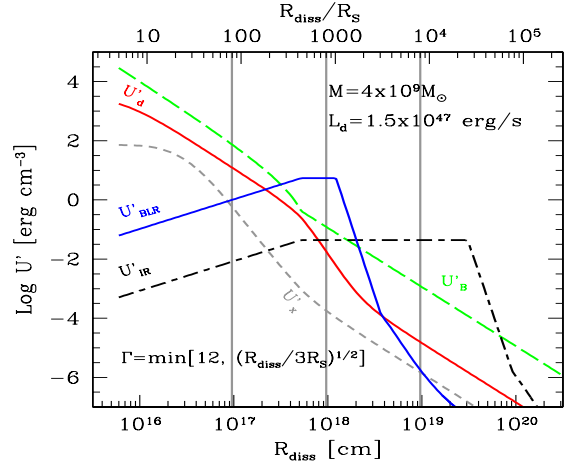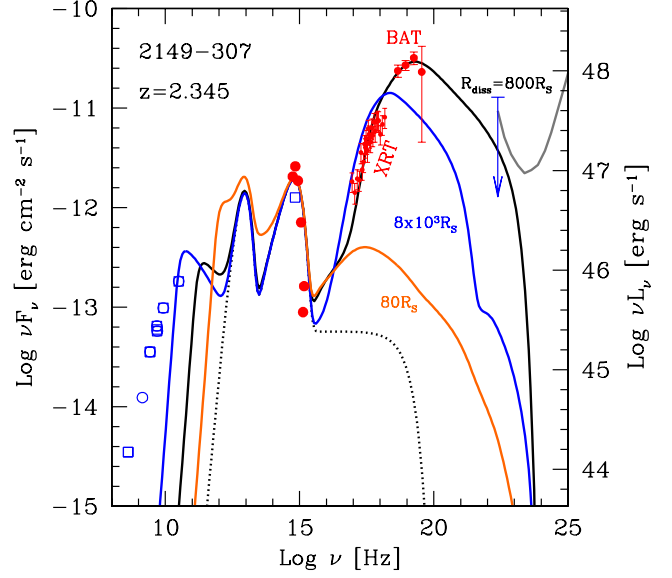
Figure 13. Top panel: the SED of one of the most distant blazars, together to 3 different models with different $R_{\rm diss}$ (see Tab. 1 for the set of parameters) to illustrate possible different states of the source. See Fabian et al. (2001) and references therein for the sources of data, and Celotti et al. (2007) for further discussion about this source.

Figure 14. Top panel: the SED PKS 2149–307 together to 3 different models (see Tab. 1 for the set of parameters) to illustrate possible different states of the source. These relatively distant, close to Eddington, high black hole mass blazars should be at the extreme of the blazar sequence, showing a high energy peak in the 100 keV–1 MeV energy band. Note that if the dissipation takes place very close to the black hole, when the jet is still accelerating and with a strong magnetic field, the resulting spectrum becomes unconspicuous at high energies, even if the intrinsic dissipated power is the same of the higher states.

of more powerful blazars, with accretion disk emitting close to the Eddington limit.

7.2   MeV blazars at large redshifts

GB 1428+4217, at $z = 4.73$, is the second most distant blazar known (the most distant is Q0906–6930, with $z = 5.47$). Its SED is shown in the top panel of Fig. 13, together with the fitting model (black line). The figure shows that this source has a prominent UV–bump, with a luminosity around 10^{47} erg s^{-1} (see also Tab. 1).

According to our model, the peak of the high energy hump of the SED during the *Beppo*SAX observations (Fabian et al. 2001) is predicted to lye at $\sim$ 1 MeV, locating this source at one extreme of the blazar sequence. The model assumes a black hole mass $M = 1.5 \times 10^9 M_\odot$, an accretion disk emitting at $\sim 2/3$ of the Eddington ratio (the other third is emitted by the X–ray corona). The dissipation region is within the BLR, at 1500 Schwarzschild

radii from the centre. The fit requires $B = 1.2$ G, corresponding to $P_{\rm B} = 5.4 \times 10^{45}$ erg s^{-1}, and $L_{\rm d} = 1.35 \times 10^{47}$ erg s^{-1}. The bottom panel of the same figures shows the radiation and magnetic energy density profiles for the parameters used to model this blazars. The mid grey vertical line corresponds to the used value of $R_{\rm diss}$. This figure shows that $U'_{\rm BLR}$ is about two orders of magnitude larger than $U'_{\rm B}$, corresponding to the ratio of the external Compton to synchrotron luminosities.

For illustration purposes, we also show the SED corresponding to increase (decrease) $R_{\rm diss}$ tenfold (see the vertical grey lines in the bottom panel, and the corresponding SED in the top panel). Shifting $R_{\rm diss}$ to $1.5 \times 10^4 R_{\rm S}$ the high energy peak moves to lower frequencies, as the relevant seed photons are softer, and at the same time the X–ray spectrum hardens. This is obtained even if the par-

ticle injection function is unchanged, and is due to the incomplete cooling occurring for the larger R_{diss} case. Since γ_{cool} shifts from 1 to ~ 34, in the X–ray band we see the emission from the un-cooled electron populations, that retains the original, "injection", slope $s = 0$. Note that the high energy peak is now slightly below 100 keV, and this would make the source even more extreme in terms of the blazar sequence. The EC to synchrotron luminosity ratio is still ~ 100, corresponding now to the ratio between U'_{IR} and U'_{B}, as can be seen in the bottom panel.

Instead, if R_{diss} is at 150 Schwarzschild radii, the SED changes more dramatically. Since in this case the bulk Lorentz factor is smaller and the magnetic field larger, the inverse Compton and synchrotron powers become comparable (see the bottom panel, showing that for this R_{diss} we have $U'_{\mathrm{B}} \sim U'_{\mathrm{d}}$). The X–ray spectrum brightens and softens considerably, in the IR–UV band the flux increases (because of the increased magnetic field) even if the bolometric observed luminosity decreases because of the decreased Doppler boosting. The fact that we did not see this kind of SED in GB 1428+4217 suggests that this state rarely occurs. This is particularly true considering that this blazars was not discovered because it was particularly bright in hard X–rays or in the γ–ray band, so there was no bias against a soft X–ray spectrum.

We lastly consider PKS 2149–307 at $z = 2.345$, as observed by the XRT and BAT instruments onboard *Swift* during its first 9 months of observations (Sambruna et al. 2007). Fig. 14 shows its SED (top panel) and the profiles of the radiation and magnetic energy densities for the considered models (bottom panels). As done for GB 1428+4217, we show what we considered the best fitting model (black line in the top panel) corresponding to $R_{\mathrm{diss}} = 9.6 \times 10^{17}$ cm, (corresponding to 800 R_{S} for the assumed black hole mass of $M = 4 \times 10^9 M_{\odot}$), and also the models corresponding to a tenfold increase (decrease) of R_{diss} (light grey lines in the top panel and vertical lines in the bottom panel). The BAT data have large error bars, precluding the possibility to firmly claim that its high energy peak is within the BAT energy range (namely, at ~ 100 keV), but this possibility is indeed suggested by the present data. The SED of this source can be explained by a set of parameters similar to the ones chosen for GB 1428+4217, and similar considerations apply. Increasing R_{diss} tenfold makes the IR radiation from the torus to dominate, leaving almost unchanged the ratio between the radiation and the magnetic energy densities (and thus the corresponding EC to synchrotron luminosity ratio). Again a decrease in R_{diss} by a factor 10 has a dramatic impact on the predicted SED, dominated in this case by the synchrotron luminosity (see also the bottom panel). However, having only data up to the medium–soft X–ray energy range, it would be almost impossible to tell what is the real appearance of the bolometric SED of the source, as almost all the changes occur above 10 keV.

8 CANONICAL JETS AND THE BLAZAR SEQUENCE

We can ask if our "canonical" jet can reproduce the phenomenological blazar sequence as proposed by Fossati et al. (1998) (see also Donato et al. 2001 and Ghisellini et al. 1998). This sequence was constructed by taking flux limited samples of blazars (in the radio and X–ray bands), dividing the sources in radio luminosity bins, and averaging the flux of the sources in each (radio luminosity) bin at selected frequencies. The resulting data are shown in Fig. 15. As discussed in Ghisellini & Tavecchio (2008) and in Maraschi et al. (2008), this sequence does not pretend to describe
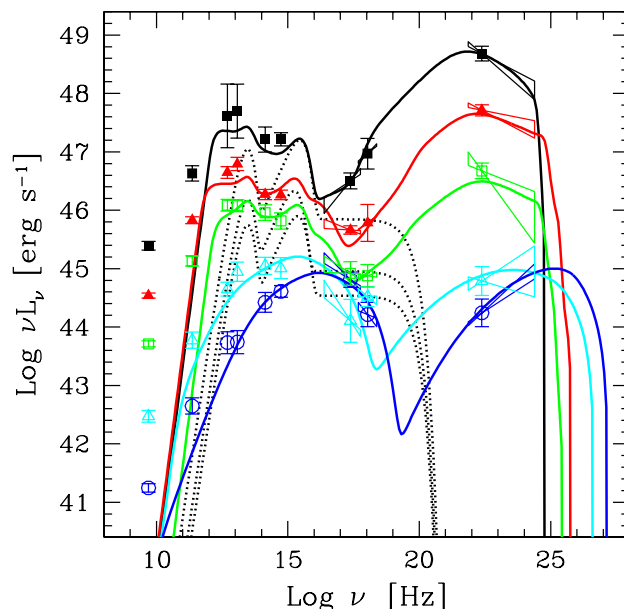
Figure 15. The blazar sequence (Fossati et al. 1998; Donato et al. 2001) interpreted in the framework of our canonical jet scenario. Parameters are listed in Tab. 1. The SED changes according to changing the accretion rate and the power of the jet, and assuming that below some critical accretion rate the accretion regime changes regime, becoming very radiatively inefficient. In out case, this occurs for the two least powerful SED, that should corresponds to low power, line–less BL Lacs.

"the average blazar", since it likely represents the most beamed sources, successfully entering in the flux limited sample they belong to. Nevertheless it is appropriate to ask if our "canonical" jet can reproduce this sequence without strong modifications of the basic assumptions. Fig. 15 then shows the SED resulting from our modelling, whose parameters are listed in Tab. 1. As can be seen the agreement is quite good, and it is achieved by assuming (as in Ghisellini & Tavecchio 2008), that the accretion disk becomes radiatively inefficient below some critical accretion rate (thus around a critical luminosity in units of the Eddington one, that we take as a few $\times 10^{-3}$). The first three, more powerful, SED correspond to sources with a standard disk, while for the two SED at lower luminosities we have "switched–off" all external radiation. The black hole mass is $3 \times 10^9 M_{\odot}$ for the two most powerful SED, and is $10^9 M_{\odot}$ for the other three. The luminosity, in the comoving frame, injected in relativistic electrons is monotonically decreasing, as the value of the magnetic field. The dissipation radius R_{diss}, in units of the Schwarzschild radius, changes slightly, but less than a factor 2.5. The energy of the injected particles need to increase as the cooling decreases. The decreased cooling also makes γ_{cool} to increase. These effects are very important for the two "BL Lac" SED, and much less for the other three most luminous SEDs.

We can conclude that the blazar sequence, as illustrated in Fig. 15, can be interpreted as a sequence of jet powers, in sources having more or less the same (large) black hole mass. The jet power correlates with the accretion disk luminosity and below some critical value the disk changes accretion regime, becoming radiatively inefficient and unable to photo–ionise the broad line clouds. A intriguing manifestation of this behavior is shown by the bright blazars recently detected by the *Fermi* satellite (Abdo et al. 2009) discussed in Ghisellini, Maraschi & Tavecchio (2009), and mirrors

what has been suggested to occur for the FRI–FRII radio–galaxy divide (Ghisellini & Celotti 2001).

9   CAVEATS

Our aim was to describe the main properties of the produced spectrum in a "canonical" jet. Specific sources can of course deviate somewhat by our description. For instance:

• Assuming $R_{\rm BLR} \propto L_{\rm d}^{1/2}$, may be approximately obeyed on average, but specific sources might behave differently. The assumed jet geometric profile and the assumption that the jet, at its start, is magnetically dominated could be two oversimplifications. We hope to test these assumptions by direct observations, since the combined efforts of the *Fermi* and *Swift* satellites can give us really simultaneous spectra on a large frequency band.

• We have assumed that the "dissipation" mechanism, converting some fraction of the jet power into radiation, has the form of an injection of primary leptons lasting for a light crossing time. With this assumption, we have derived the particle distribution at this time, which corresponds to the maximum produced flux. However, the injection can last for a longer or shorter time. Our framework is appropriate for describing a "snapshot" of the SED, and not for a time–dependent analysis.

• We assume that the magnetic field in the dissipation region is the same as the magnetic field transported by the jet. It is not amplified by e.g. shocks, nor it is reduced by e.g. reconnection events (see e.g. Giannios, Uzdensky & Begelman 2009). Although we can assume any value of the magnetic field in the dissipation region (i.e. we can fix any value in the numerical code calculating the SED), we prefer this choice for all the examples shown, because of simplicity.

• We focused on high power blazars, thought to have "standard" accretion disks and broad line regions, and therefore we did not discuss in detail the expected SED from low power (and TeV emitting) BL Lacs. However, we could simply extend our study to these sources if we "switch–off" the external radiation components, as expected if the accretion disk becomes radiatively inefficient, making very weak or absent broad emission lines. In Fig. 15 we indeed show two examples of the expected spectra in this case.

• All the shown SED do not take into account the absorption of γ–rays due to the IR, optical and UV background, but only the "internal" absorption caused by the radiation fields existing close to the emitting blob.

• We have always assumed a relatively small viewing angle ($\theta_{\rm v} \sim 3°$), of the same order of $1/\Gamma$. Since Γ and $\theta_{\rm v}$ are two separated input parameters, we could change $\theta_{\rm v}$ (and thus the Doppler factor δ) for a fixed Γ. However, this would introduce a delicate issue, since the external radiation field, in the comoving frame, is not isotropic. If the emitting blob is inside the BLR, for instance, then all external photons appear to come from one direction, and we could apply the formalism of Dermer (1995) to describe the pattern of the scattered radiation. Note that, in this case, if $\theta_{\rm v} = 1/\Gamma$ (and thus $\delta = \Gamma$) one has the observed luminosity as for radiation isotropic in the rest frame. On the other hand, if the emitting region is beyond the BLR, then the arrival directions of the BLR external photons are spread, and it is not trivial to reconstruct the exact pattern. But in this cases the BLR component is hardly dominant with respect to the IR radiation from the torus. We have decided, for simplicity, to use $\theta_{\rm v} \sim 1/\Gamma$, and to treat the emitted radiation pattern is the same way as for an isotropic seed photon distribution.

• We neglected, for simplicity, the possibility of a jet composed by a fast spine surrounded by a slower layer. This structured jet have been proposed for low power BL Lacs and FR I radio–galaxies (Ghisellini, Tavecchio & Chiaberge 2005), and can ease some problems in explaining the SED properties in these sources. While in high power blazars there is no compelling need, yet, for such a structure, its inclusion in the present study would make our description much more complex and model–dependent, given the freedom to choice the parameters for the layer emission.

• For simplicity, we neglected the possibility that the BLR and the associated inter–cloud material can absorb and re-emit, or scatter, part of the synchrotron radiation produced by the jet (i.e. the "mirror model", see Ghisellini & Madau 1996, and some criticism by Bednarek 1998; Böttcher & Dermer 1998).

• The jet, even if cold (i.e. before dissipation), is relativistic, and the carried leptons could scatter the external radiation by bulk Comptonization. This process, proposed by Begelman & Sikora (1987) and Sikora et al. (1994) and studied in detail in Celotti, Ghisellini & Fabian (2007), could produce a black–body like component in the X–ray band, whose level depends on how the jet accelerates and on the amount of leptons carried by the jet. We have neglected this component for simplicity, although it can be a very important diagnostic for deriving, at the same time, the bulk Lorentz factor of the jet and its matter content.

10   CONCLUSIONS

The relatively recent observations of blazars, especially in the γ–ray band, have disclosed some of the crucial ingredient for our understanding of jets, namely the bolometric power output and the real shape of the produced SED. Although there is still discussion about the origin of the high energy emission of blazars, the relatively simple one–zone leptonic model was rather successful to interpret the existing data of specific sources.

In this paper, rather than modelling single sources, we tried to propose a more general description of the emission produced by high power jets. For this aim we have first summarised in a simple way the expected radiation fields as a function of the distance from the black hole, and then we have studied how the expected SED changes if the main dissipation occurs at different locations in the jet. We have done this by assuming rather reasonable prescription for the accretion disk and its X–ray corona emission, and using reasonable prescriptions for the radiation fields corresponding to the broad line region and the infrared torus. We have also assumed that the jet conserves its Poynting flux at all distances, thus fixing the profile of the magnetic field. Since all these prescriptions correspond to rather uncontroversial assumptions, we believe that they should well characterise the properties of an average, canonical, large power jet.

The main conclusions of our work are:

• The magnetic energy density is always smaller than the external radiation energy densities, except at the very beginning of the jet and at the kpc scale. Beyond these scales, the contribution of the cosmic microwave background becomes dominant.

• The inclusion of the X–ray radiation from the disk corona allowed to quantify the effect of pair production and reprocessing for small $R_{\rm diss}$. This is found to be severe if the primary spectrum emits most of its power at energy above the pair production threshold. This requires that the bulk Lorentz factor is large even in the very vicinity of the black hole. In this case there is a transfer of power from the γ–ray to the X–ray band. Our quantitative

analysis confirms earlier, more qualitative, statements concerning the non–dissipative nature of the inner (i.e. up to a few hundreds Schwarzschild radii) jet.

• If instead the jet accelerates gradually (i.e. as $\Gamma \propto R^{1/2}$ up to a maximum value), the magnetic energy density dominates the cooling at the start of the jet, resulting in a synchrotron dominated SED, with a very small fraction of power being emitted above the pair production energy threshold. These SED would hardly be detectable, since the small Γ means a much reduced Doppler enhancement of the flux, and thus these components are easily overtaken by the emission at larger distances (that have a larger Γ). In any case, early dissipation (i.e. small $R_{\rm diss}$) is not an efficient process to create electron–positron pairs.

• Besides the inner part of the jet, the "internal" pair absorption (i.e. calculated within the emitting blob) can be particularly important also if dissipation takes place close to (but within) the BLR and close to (but within) $R_{\rm diss} \sim R_{\rm IR}$. In these cases, however, a small fraction of the emitted power can be absorbed, and the reprocessing is modest.

• The Klein–Nishina decrease (with energy) of the scattering cross section imprints a characteristic steepening in the spectrum above ~ 10 GeV if the dissipation takes place within the BLR, and at ~ 1 TeV if the dissipation occurs beyond the BLR but within $R_{\rm IR}$.

• The above point has important consequences on the possible use of the high energy (GeV) data of blazars to study the optical–UV background. In fact the signature of the γ–γ absorption due to this component would be a rather sharp steepening of the received spectrum, that would be very similar to the intrinsic steepening of the primary spectrum due to Klein–Nishina effects *if most of the dissipation takes place within the BLR*. In this case also the "internal" γ–γ absorption due to BLR photons will be relevant. It will be very difficult to disentangle these effects. On the other hand, if the observed spectrum continues unbroken above $15(1 + z)$ GeV, we can infer that most of the dissipation has occurred beyond $R_{\rm BLR}$. In this case both Klein–Nishina and "internal" absorption effects are unimportant up to the TeV band. These therefore would be the best candidates to study the opt–UV cosmic backgrounds.

• The magnetic field decreases with distance, while the $U'_{\rm BLR}$ is approximately constant up to $R_{\rm BLR}$, and $U'_{\rm IR}$ is approximately constant up to $R_{\rm IR}$. At these distances (i.e. $R_{\rm diss} \sim R_{\rm BLR}$ and $R_{\rm diss} \sim R_{\rm IR}$) the Compton dominance is very large. Existing observations of large power blazars already indicate that these blazars are characterised by a weak synchrotron component, a strong thermal, disk component (unhidden by the synchrotron flux) and a very large high energy flux. These are the sources with the largest Compton dominance, strongly suggesting that $R_{\rm diss}$ is relatively large (i.e. close to the $R_{\rm BLR}$ or $R_{\rm IR}$). This helps to understand why in these sources the soft X–rays are relatively weak and very hard, demanding a very weak SSC flux: since the magnetic field is small, not only the synchrotron, but also the SSC flux is small with respect to the EC radiation.

• Concerning the above point, the fact that the high power blazars we already know of have the mentioned properties does not imply that they preferentially dissipate at large distances with respect to less powerful sources, since we may have selected them on the basis of their hard X–ray or γ–ray flux (therefore taking advantage of the large Compton dominance they have when $R_{\rm diss}$ is large). In other words: they may dissipate at different $R_{\rm diss}$ at different times, but we select them only when $R_{\rm diss}$ is large.

• Although most of the dissipation should take place in one zone of the jet (with $R_{\rm diss} \sim 500$–1000 $R_{\rm S}$), it is very likely that dissi-

pation occurs also at larger distances, albeit with less power. The flux originating in these zones can be important in some frequency bands, as the soft X–ray one, with important consequences on the observed variability. Instead, in the γ–ray energy band (at least when the γ–ray dominates the bolometric output) most of the flux should originate in one zone.

• Blazars with large masses should be characterised by the largest inverse Compton to synchrotron ratios, and thus they will be well represented in γ–ray all sky surveys, as performed by the *Fermi* satellite.

• The most powerful blazars, with the most powerful associated accretion disk, should have a high energy hump peaking in the 100 keV–1 MeV energy range. The exact location of the peak frequency depends somewhat on $R_{\rm diss}$, being smaller if dissipation occurs beyond the BLR. These blazars should form the high power extension of the blazar sequence. They *are not* easily detectable by the *Fermi* satellite, since their MeV peak implies relatively small fluxes in the GeV band. The brightest of them have already been revealed by the serendipitous survey of the BAT instrument onboard *Swift*.

• The phenomenological blazar sequence as presented in Fossati et al. (1998) can be interpreted as a sequence of "canonical jets" in sources with more or less the same (large) black hole mass, but with different accretion rates and different jet powers.

REFERENCES

Aharonian F.A., 2000, New Astronomy, 5, 377

Albert J., Aliu E., Anderhub H. (The MAGIC Collaboration) et al., 2008, Sci, 320, 1752

Ballo L., Maraschi L., Tavecchio F. et al., 2002, ApJ, 567, 50

Bednarek W., 2008, A&A, 336, 123

Begelman M.C. & Sikora M., 1987, ApJ, 322, 650

Bentz M.C., Peterson B.M., Pogge R.W., Vestergaard M. & Onken C., 2006, ApJ, 644, 133

Bentz M.C., Peterson B.M., Netzer H., Pogge R.W. & Vestergaard M., 2008, subm. to ApJ (astro–ph/0812.2283)

Blandford R. & Levinson A., 1995, ApJ, 441, 79

Błazejowski M., Sikora M., Moderski R. & Madejski G.M., 2000, ApJ, 545, 107

Bloom S.D. & Marscher A.P. 1996, ApJ, 461, 657

Bonning E.W., Bailyn C., Urry C.M., et al., subm to ApJ Letters (astro–ph/0812-4582)

Böttcher M., 2007, Ap&SS, 309, 95

Böttcher M. & Dermer C., 1998, ApJ, 501, L51

Celotti A., Ghisellini G. & Fabian A.C., 2007, MNRAS, 375, 417

Celotti A. & Ghisellini G., 2008, MNRAS, 385, 283

Celotti A., Ghisellini G. & Chiaberge, 2001, MNRAS, 321, L1

Cleary K., Lawrence C.R., Marshall J.A., Hao L. & Meier D., 2007, ApJ, 660, 117

Dermer C.D. & Schlickeiser R., 1993, ApJ, 416, 458

Dermer C.D., 1995, ApJ, 446, L63

Dermer C.D., Finke J.D., Krug H. & Boettcher M., 2009, ApJ, 692, 32

Donato D., Ghisellini G., Tagliaferri G. & Fossati G., 2001, A&A, 375, 739

Fabian A.C., Celotti A., Iwasawa K. & Ghisellini G., 2001, MNRAS, 324, 628

Fossati G., Maraschi L., Celotti A., Comastri A. & Ghisellini G., 1998, MNRAS, 299, 433

Ghisellini G., 1989, MNRAS, 238, 449

Ghisellini G., Celotti A., Fossati G., Maraschi L. & Comastri A., 1998, MNRAS, 301, 451

Ghisellini G. & Madau P., 1996, MNRAS, 280, 67

Ghisellini G. & Celotti A., 2001, A&A, 379, L1

Ghisellini G., Tavecchio F. & Chiaberge M., 2005, A&A, 432, 401

Ghisellini G. & Tavecchio F., 2008, MNRAS, 387, 1669

Ghisellini G., Maraschi L. & Tavecchio F., 2009, MNRAS, in press (astro–ph0903.2043)

Giannios D., Uzdensky D.A. Begelman M.C., 2009, subm to MNRAS (astro–ph/0901.1877)

Kaspi S., Brandt W.N., Maoz D., Netxer H., Schneider D.P. & Shemmer O., 2007, ApJ, 659, 997

Katarzynski K. & Ghisellini G., 2007, A&A, 463, 529

Komissarov S.S., Barkov M.V., Vlahakis N. & Kñigl A., 2007, NMNRAS, 380, 51

Liu H.T., Bai J.M. & Ma L., 2008, ApJ, 688, L148

Mannheim K., 1993, A&A, 269, 67

Maraschi L., Ghisellini G. & Celotti A., 1992, ApJ, 397, L5

Maraschi L., Foschini L., Ghisellini G., Tavecchio F. & Sambruna R.M., 2008, MNRAS, 391, 1981

Mücke A. & Protheroe R.J.. 2001, Astroparticle Physics, 15, 121

Mücke A., Protheroe R.J., Engel R., Rachen J.P. & Stanev, T., 2003, Astroparticle Physics, 18, 593

Nenkova M., Sirocky M.M., Ivezic Z. & Elitzur M., 2008, ApJ, 685, 147

Pian E., Urry C.M., Maraschi L., et al., 1999, ApJ, 521, 112

Primack J.R., Bullock J.S. & Somerville R.S., 2005, AIPC, 745, 23

Sambruna R.M., Tavecchio F., Ghisellini G., Donato D., Holland S.T., Markwardt C.B., Tueller J. & Mushotzky R.F., 2007, ApJ, 669, 884

Shakura N.I. & Syunyaev, R.A., 1973, A&A, 24, 337

Sikora M., Begelman M.C. & Rees M.J., 1994, ApJ, 421, 153

Sikora M. & Madejski G., 2000, ApJ, 534, 109

Sikora M., Błazejowski M., Moderski R. & Madejski G.M., 2002, ApJ, 577, 78

Sitarek J. & Bednarek W., 2008, MNRAS, 391, 624

Stawarz Ł., Sikora M. & Ostrowski M., 2003, ApJ, 2003, 597, 186

Svensson R., 1987, MNRAS, 227, 403

Tavecchio F., Maraschi L., Sambruna R.M. & Urry C.M., 2000, ApJ, 544, L23

Tavecchio F. & Ghisellini G., 2008, MNRAS, 386, 945

Tavecchio F. & Mazin D., 2009, MNRAS, 392, L40

Vlahakis N. & Königl A., 2004, ApJ, 605, 656